REPORT DOCUMENTATION PAGE

Form Approved
OMB No. 0704-0188

1. REPORT DATE *(DD-MM-YYYY)*	2. REPORT TYPE	3. DATES COVERED *(From - To)*
01-01-2010	REPRINT	

4. TITLE AND SUBTITLE
Solar wind structure sources and periodicities of auroral electron power over three solar cycles

5a. CONTRACT NUMBER

5b. GRANT NUMBER

5c. PROGRAM ELEMENT NUMBER
62601F

6. AUTHOR(S)
B.A. Emery*, I.G. Richardson**, D.S. Evans# and F.J. Rich

5d. PROJECT NUMBER
1010

5e. TASK NUMBER
SD

5f. WORK UNIT NUMBER
A1

7. PERFORMING ORGANIZATION NAME(S) AND ADDRESS(ES)

Air Force Research Laboratory
29 Randolph Road
Hanscom AFB MA 01731-3010

8. PERFORMING ORGANIZATION REPORT NUMBER

AFRL-RV-HA-TR-2010-1006

9. SPONSORING / MONITORING AGENCY NAME(S) AND ADDRESS(ES)

10. SPONSOR/MONITOR'S ACRONYM(S)

AFRL/RVBX

11. SPONSOR/MONITOR'S REPORT NUMBER(S)

12. DISTRIBUTION / AVAILABILITY STATEMENT
Approved for Public Release; Distribution Unlimited
*High Altitude Observatory, NCAR, Boulder, CO, **Goddard Space Flt Ctr, NASA, Greenbelt, MD
#Space Weather Prediction Ctr, NOAA, Boulder, CO

13. SUPPLEMENTARY NOTES
REPRINTED FROM: Journal of Atmospheric and Terrestrial Physics, 71 (2009), 1157-1175
doi: 10.1016/j.jastp.2008.08.005

14. ABSTRACT

We assess the contributions of various types of solar wind structures (transients, coronal hole high-speed streams (HSS), and slow-speed wind) to hourly average auroral electron power (P_e). The time variation of the solar wind velocity (V_{sw}) and P_e are determined by HSS, which contribute ~47% to P_e and V_{sw}. Transients contribute ~42% of P_e in solar maxima, and ~6% in solar minimum. Cross-correlations of P_e with $V_{sw}|B|$ for negative B_z are significant. P_e exhibits solar rotational periodicities similar to those for V_{sw}, with strong 7- and 9-day periodicities in 2005–2008 and equinox semiannual periodicities in 1995–1999.

15. SUBJECT TERMS
Electron auroral energy fluxes
Solar cycle variations
Solar wind speed structures
Periodicities

16. SECURITY CLASSIFICATION OF:			17. LIMITATION OF ABSTRACT	18. NUMBER OF PAGES	19a. NAME OF RESPONSIBLE ERSONS
a. REPORT	b. ABSTRACT	c. THIS PAGE			F. Rich
UNCLAS	UNCL		SAR		19b. TELEPHONE NUMBER *(include area code)*

Journal of Atmospheric and Solar-Terrestrial Physics 71 (2009) 1157–1175

Contents lists available at ScienceDirect

Journal of Atmospheric and Solar-Terrestrial Physics

journal homepage: www.elsevier.com/locate/jastp

Solar wind structure sources and periodicities of auroral electron power over three solar cycles

Barbara A. Emery [a,*], Ian G. Richardson [b,c], David S. Evans [d], Frederick J. Rich [e,1]

[a] High Altitude Observatory/NCAR, Boulder, CO, USA
[b] Goddard Space Flight Center/NASA, MD, USA
[c] University of Maryland, MD, USA
[d] Space Weather Prediction Center/NOAA, Boulder, CO, USA
[e] Air Force Geophysics Laboratory, MA, USA

ARTICLE INFO

Article history:
Accepted 11 August 2008
Available online 30 August 2008

Keywords:
Electron auroral energy fluxes
Solar wind speed structures
Solar cycle variations
Periodicities

ABSTRACT

We assess the contributions of various types of solar wind structures (transients, coronal hole high-speed streams (HSS), and slow-speed wind) to hourly average auroral electron power (P_e). The time variation of the solar wind velocity (V_{sw}) and P_e are determined by HSS, which contribute ~47% to P_e and V_{sw}. Transients contribute ~42% of P_e in solar maxima, and ~6% in solar minimum. Cross-correlations of P_e with $V_{sw}|B|$ for negative B_z are significant. P_e exhibits solar rotational periodicities similar to those for V_{sw}, with strong 7- and 9-day periodicities in 2005–2008 and equinox semiannual periodicities in 1995–1999.

1. Introduction

One of the methods of estimating auroral activity is to derive the hemispheric power (HP), which is the area-integrated particle energy deposition into each high-latitude hemisphere (Fuller-Rowell and Evans, 1987). Statistical patterns of electron and ion energy influx from Defense Meteorological Satellite Program (DMSP) satellites were made as a function of K_p by Hardy et al. (1985, 1989), and patterns of the total (electron and ion) energy input from National Oceanic and Atmospheric Administration (NOAA) satellites were made as a function of HP by Fuller-Rowell and Evans (1987). We use the intersatellite-adjusted global (sum of both hemispheres) electron hemispheric power (HP_e) described by Emery et al. (2005, 2006, 2008) to investigate the relationship between solar cycle variations in the auroral electron power (P_e) and the varying fractions of the various types of structures in the solar wind (coronal hole flows, transients associated with coronal mass ejections (CME) at the Sun, and slow solar wind) through the solar cycle (SC). The aim is to explain the large variability in HP_e exhibited over three different ~11-year solar activity cycles by Emery et al. (2006, 2008).

The highest cross-correlations of HP_e are with the 3-h geomagnetic activity indices of K_p and a_p, where a_p is a linearization of the K_p index. Emery et al. (2008) showed that the cross-correlations of daily average Southern Hemisphere HP_e were 0.87 and 0.83 for daily K_p and A_p, respectively. (The correlations decreased by ~0.17 when hourly values were used.) The high cross-correlations with K_p and A_p are not surprising since the auroral inputs, along with solar conductance on the dayside, create the auroral current systems measured as deviations in the magnetic field at ground stations which lead to the K_p index. The present study will examine cross-correlations of hourly P_e with solar wind parameters such as the solar wind velocity (V_{sw}), the interplanetary magnetic field (IMF) magnitude (|B|), the B_z component, and various combinations in the context of different solar wind structures.

The ultimate driver of the auroral precipitation is the Sun via the solar wind. The solar wind brings 'frozen-in' magnetic field lines from the Sun to the Earth. If the IMF is

* Corresponding author.
E-mail address: emery@hao.ucar.edu (B.A. Emery).
[1] Present address: Lincoln Laboratory, MIT, MA, USA.

1364-6826/$ - see front matter © 2008 Elsevier Ltd. All rights reserved.
doi:10.1016/j.jastp.2008.08.005

directed southwards (B_z negative), or anti-parallel to the Earth's external magnetic field, then the two different magnetic fields can merge and allow direct access of the solar wind to the Earth's magnetosphere and ionosphere. Southward IMF (negative IMF B_z) results in increased aurora, stronger polar cap potential drops, and stronger currents in the ionosphere (e.g. Reiff and Luhmann, 1986).

Magnetic reconnection is the way mass, momentum and energy are transferred from the solar wind and IMF into the magnetosphere–ionosphere–atmosphere system. Most reconnection is quasi-stationary on the dayside of the magnetopause (e.g. Raeder, 2006), but some reconnection is time-dependant and patchy, such as that experienced by flux transfer events (FTE) under strong southward IMF conditions (Bz negative) in the winter hemisphere due to the dipole tilt at solstice between two X-lines (Raeder, 2006). Other FTEs can develop with strong IMF Bx or By at other times in other locations. Observations by multiple satellites (e.g. Hasegawa et al., 2006; Lui et al., 2008) show these FTEs as frozen-in twisted bundles of magnetic fields or ropes that can be as wide as the Earth, which last only a few minutes as they deliver the solar wind particles flowing along these ropes to the magnetosphere.

The cold solar wind electrons from FTEs or from regular quasi-steady reconnection on the dayside magnetopause are then energized in the Earth's magnetotail and are deposited in the high-latitude auroral regions in upward field-aligned currents (FACs) (e.g. Iijima and Potemra, 1976). Discrete electrons are accelerated downwards within Region 1 FACs in the pre-midnight sector towards the poleward edge of the aurora, while the more common diffuse electron aurora caused by hot plasma sheet electrons are pitch-angle scattered into the loss cone by whistler mode waves near the equatorial plane and precipitated into mostly the post-midnight sector (e.g. Hamrin et al., 2005), creating the Region 2 upward FACs (e.g. Shue et al., 2001). The time needed to energize the auroral electrons in the Earth's magnetosphere is about 1 h, since cross-correlations of the estimated auroral energy flux and the IMF or solar wind velocity are maximized with a 1 h lag (see Section 3.4).

The most common period found in solar wind and geomagnetic activity parameters is ~27 days, or the equatorial rotation period of the Sun as viewed from the Earth (e.g. Svalgaard and Wilcox, 1975; Gosling et al., 1976, 1977). Another prominent period is associated with the ~11-year solar cycle (SC). Each SC starts at solar (sunspot) minimum, although the solar magnetic dipole field reverses just after solar maximum. The change in magnetic polarity discovered by Hale and Nicholson (1925) produces a 22-year solar magnetic cycle (the Hale cycle), which starts with an even SC and ends with an odd SC. Javaraiah et al. (2005) present evidence of the equatorial rotation rate and the latitudinal gradient of the rotation rate from sunspots that suggest that the basic physical cycle of the Sun is the 22-year magnetic cycle rather than the 11-year activity cycle. Cliver et al. (1996) showed that the sunspot numbers are highest in the ending odd SCs in the even–odd Hale pairs over the last 150 years starting with SC 10 in 1857. However, this pattern was broken in SC 23 as shown in the bottom panel of Fig. 1a, when the sunspot number in SC 23 was less than that for SC 22 in the most recent Hale cycle. The last time this happened was in the Hale cycle for SC 8 (maximum in 1837) and SC 9 (maximum in 1848), although it happened also in the 4–5 Hale cycle and several times before 1760 when the sunspot data quality is 'questionable' or 'poor' (e.g. Cliver et al., 1996).

Our study investigates the periodicities in V_{sw} and in the global auroral electron power (P_e). The differences and similarities of P_e in odd and even SCs are also examined and compared with previous studies of the 22-year variation in the geomagnetic activity index *aa* by Cliver et al. (1996), who showed maximum *aa* activities between declining even cycles and ascending odd cycles. However, like the sunspot numbers, this *aa* pattern was broken in the latest Hale cycle, when the yearly *aa* index reached a maximum of 38 in 2003 during the declining phase of SC 23. This yearly *aa* maximum in 2003 exceeded all other yearly values in the last four solar cycles (Fig. 1 of Kozyra et al., 2006).

In this study, we consider the solar wind to be composed of three main types of flows: slow speed, coronal hole (CH) high-speed streams (HSS), and transients. The slow-speed wind velocity ($V_{sw} < \sim 400$ km/s) comes from the borders of coronal holes (e.g. Maris and Maris, 2005) and from the region of the equatorial streamer belt. Coronal holes are found at both high and low latitudes on the Sun, where the polar CHs are more prominent during solar minimum. The low-latitude CHs give rise to the corotating HSS seen at Earth, which are particularly prominent in the descending and minimum phases of the solar cycle. Typically, there are two CHs of opposite polarity, which give rise to a two-stream magnetic sector structure (IMF B_x positive and negative) in the ecliptic with magnetic activity on Earth recurring every 27 days and also every ~13.5 days because of the two streams. However, there are periods when there are more than two CHs, such as described by Temmer et al. (2007) where three CHs produced strong 9-day periodicities in V_{sw} in 2005.

The third type of flows is associated with CME. These include interplanetary coronal mass ejections (ICMEs, e.g., Cane and Richardson, 2003 and references therein) and the sheath of compressed solar wind formed upstream of many ICMEs that is often bounded by a shock at the leading edge. Magnetic clouds are a subset of ICMEs where the IMF magnitude is large and the field direction changes slowly through a large angle. Magnetic clouds are often responsible for the most intense geomagnetic storms (e.g., Zhang et al., 2007). Li and Luhmann (2004) found that the occurrence frequency of bipolar magnetic clouds changes from north to south in even SCs to south to north in odd SCs, where the polarity change occurs late in the descent phase of the SC.

According to Berdichevsky et al. (2005), ~8% of ICMEs between 1996 and 2002 were embedded in HSS. More commonly, ICMEs are found near HSS leading edges, or in slow interstream solar wind. Watari and Watanabe (2000) reported about half of the magnetic disturbances (minimum $D_{st} < -50$ nT) in the solar minimum years of 1995–1997 were associated with ICMEs, and that almost

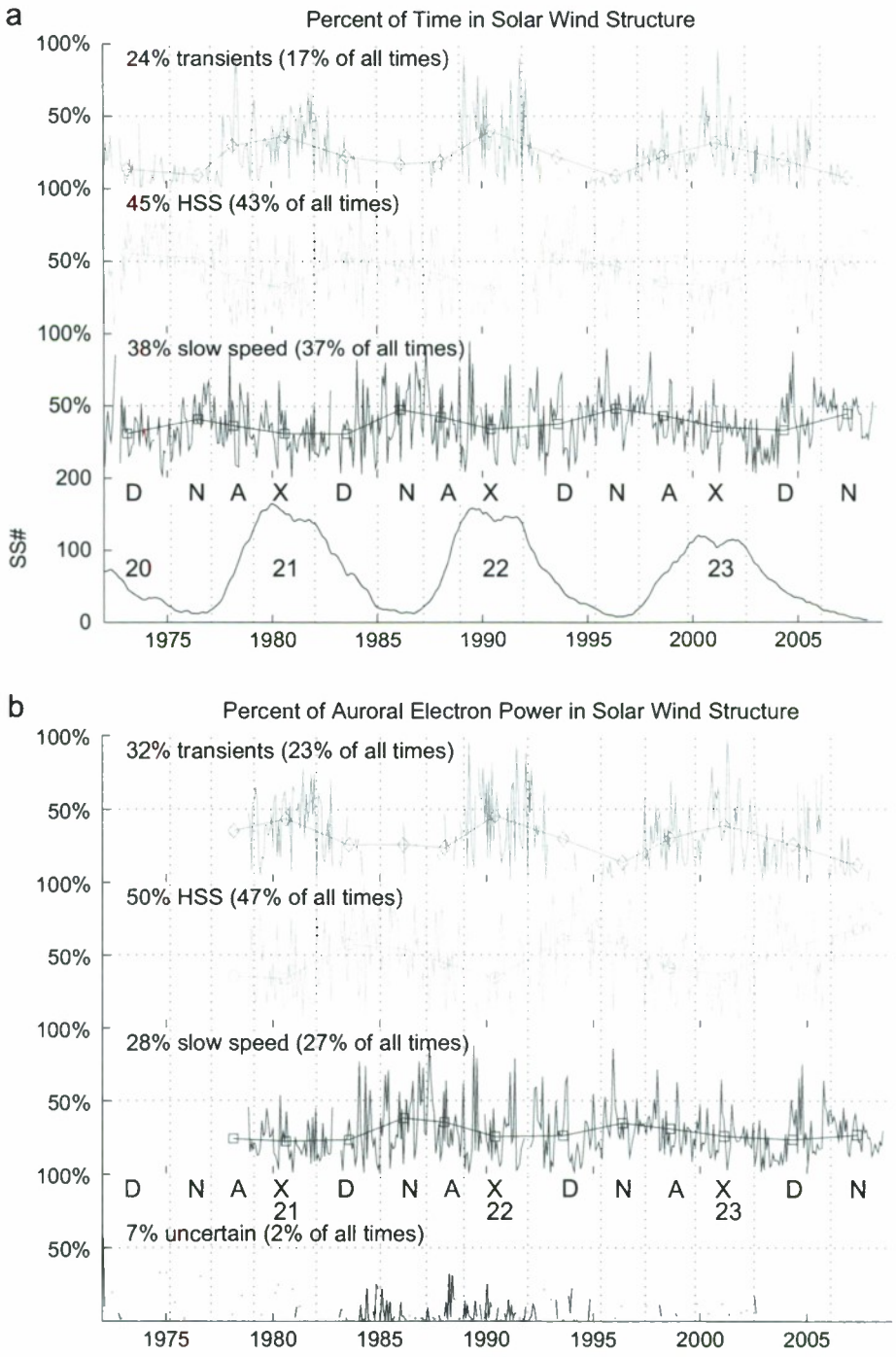

Fig. 1. (a) The fraction of time that is spent in each kind of solar wind structure from January 1972 to August 2008 for hourly average values plotted as 27-day averages. Only hours with both V_{sw} and IMF data are considered. The percentages in the labels give the average fraction of time spent in each structure type for 27-day periods where the structure is present, or for all times. The monthly smoothed sunspot number is plotted with dotted lines to delineate each phase of the solar cycle (minimum, ascent, maximum, and descent), where the means in each phase are plotted as symbols linked with straight lines. (b) Same as (a) for the fraction of P_e deposited hourly by specific solar wind structures from November 1978 where only hours with HP_e, V_{sw}, and IMF are considered. P_e lags V_{sw} and IMF by 1 h. The 'uncertain' type of solar wind structure is plotted at the bottom.

half of these ICMEs were propagating through HSS. All of their stronger storms (minimum $D_{st}<-100$ nT) were either definitely or possibly associated with ICMEs. Richardson et al. (2001) reported that 97% of the major K_p storms ($K_p>8$-) from 1972 to 2000 were associated with ICMEs, while half or more of any storms with K_p 5- or higher were associated with ICMEs during solar maximum.

The present study examines the relationship between the hourly solar wind structures and the electron auroral precipitation as described by the intersatellite-adjusted electron hemispheric power (HP_e) from Emery et al. (2005, 2006, 2008) summed over both hemispheres (P_e) Cross-correlations are found between various structure types, P_e, V_{sw} and IMF. The periodicities in P_e during various parts of the SC are examined to help explain the source of P_e deposition over time and the large variety seen in P_e over three solar cycles.

2. Data analysis

Using the total statistical patterns of HP, David Evans (private communication) computed *HP* from single satellite passes. This calculation was adapted to estimate just the electron hemispheric power (HP_e) from both NOAA and DMSP satellites (David Evans, private communication and William Denig, private communication). Of course, imagers with most of the auroral oval in their field-of-view can make the best HP_e estimates (e.g. Lummerzheim et al., 1997; Hubert et al., 2002; Zhang and Paxton, 2008; Luan et al., 2009). However, the longest dataset of HP_e estimates is from single-pass NOAA and DMSP satellites that have been intercalibrated and cleaned up by Emery et al. (2005, 2006, 2008). We use HP_e estimates instead of *HP* estimates because only HP_e estimates are available from DMSP satellites. Ions contribute ~10% to *HP* from NOAA satellites (e.g. Hubert et al., 2002; Emery et al., 2008) and have different characteristics from electrons.

We use average hourly estimates of HP_e from both hemispheres from day 306 (2 November) 1978 (78306) to day 225 (12 August) 2008 (08225). P_e is the sum of HP_e in the Southern Hemisphere and in the Northern Hemisphere. When one hemisphere is absent, P_e is estimated as twice the HP_e from the available hemisphere. P_e is used in order to eliminate the seasonal variations found in HP_e (Emery et al., 2008), where the summer HP_e values are larger than the winter values for low-magnitude HP_e, while the winter HP_e values are larger than summer for moderate and high magnitudes of HP_e.

The magnitude of HP_e or P_e used in the present study could be increased by a factor of two since the Emery et al. (2008) HP_e estimates as a function of K_p are approximately half the Zhang and Paxton (2008) TIMED/GUVI image HP estimates in their Fig. 8. Zhang and Paxton (2008) show that DMSP electron energy fluxes agree with GUVI images at the location of the satellite crossings, but that the DMSP HP estimates are smaller than the GUVI estimates. They discuss several possible reasons for this, but another reason could be that DMSP or NOAA averaged energy flux patterns are low because of averaging. However, the variations in P_e over time should be good, even if the magnitudes are relatively low.

We compare the P_e data with a classification of the hourly solar wind structures at Earth during 1972–2008, which is an update of that used by Richardson et al. (2000, 2002). Near-Earth, 1-h averaged solar wind plasma and magnetic field data from the Space Physics Data Facility OMNI database are used to classify the solar wind into three types of structures:

(1) Transient structures, in particular ICMEs, believed to be the counterparts of CMEs at the Sun and the associated upstream sheaths of compressed solar wind. The in-situ signatures of ICMEs, which can help to identify such structures are summarized, for example, by Zurbuchen and Richardson (2006). For cycle 23, we base the classification on an updated and extended version of the ICME list of Cane and Richardson (2003), but also include sheath flows following interplanetary shocks that do not include an encounter with an ICME. Interplanetary shocks are more extended than the driving ICMEs (e.g., Borrini et al., 1982; Cane, 1988). For earlier cycles, similar identifications have been made and used in various studies (e.g., Cane et al., 1996; Richardson and Cane, 1993, 1995; Richardson et al., 1997). Jian et al. (2006b) have also compiled lists of ICMEs and discussed their identification criteria.
(2) Corotating high-speed solar wind streams from coronal holes. As described by Belcher and Davis (1971), these HSS are characterized by an increase in solar wind speed at the leading edge over the order of a day, followed by a slower decay lasting for one to several days. The interaction of the stream leading edge with the slower preceding solar wind generates a region of dense plasma with enhanced magnetic fields, the corotating interaction region (CIR), at the stream leading edge.
(3) Interstream, slow-speed ($<\sim$400 km/s) solar wind.

A fourth category includes periods in which the classification is 'uncertain' because of insufficient or unavailable solar wind observations. This is a particular problem between late 1982 and 1994 when the OMNI data are predominantly from IMP 8, which was located in the solar wind for only ~60% of each orbit.

On occasion, other data sources can fill in. For example, geomagnetic sudden storm commencements (SSC) can help identify interplanetary shocks that are often associated with ICMEs, while cosmic ray depressions can indicate the presence of ICMEs and HSS (e.g., Richardson et al., 1996). For further details of the classification, see Richardson et al. (2000). In addition to the studies noted above, Jian et al. (2006a) have catalogued what they describe as "Stream interaction regions" in solar cycle 23. For earlier cycles, HSS are listed by Lindblad et al. (1989) and Mavromichalaki and Vassilaki (1998), but these include both corotating HSS from coronal holes (CH-HSS) and transient flows, the latter listed as "flare-generated" high-speed streams (FG-HSS).

3. Solar wind structures and auroral electron power

3.1. Contribution of different types of solar wind structure to auroral precipitation

Fig. 1a shows the time spent in each solar wind structure using hourly solar wind structure classifications

from 1 January 1972 to 2 August 2008 for hours when V_{sw} and IMF are available (276611 h or 69% of the time) plotted as 27-day averages. The two percentages written above each graph are first the mean of the plotted 27-day averages, while the second percentage represents the fraction of time that type of solar wind structure is present for all available 27-day periods, where 'available' excludes 27-day periods of missing data, but includes periods when the specified structure is absent. The biggest difference in percentages is for the transient flows because transients are absent in 29% of the available 27-day periods, thus dropping the total fraction of time transients are present from 24% to 17% of all times.

The bottom plot shows the smoothed monthly sunspot number. We use the definitions of Maris and Maris (2005) for SCs 20–22, where the minimum (N) is defined by the months where the monthly smoothed sunspot number is less than 20 and the 'shape' of the maxima (X) is included above varying limits of the monthly smoothed sunspot number. Thus, we define the SC 23 maximum to be encompassed in the interval with monthly smoothed sunspot numbers greater than 103. The ascent (A) and descent (D) phases of the SC are the intervals in-between the minima and maxima. These four phases of each sunspot cycle are denoted by dashed lines in Fig. 1a. Note that the plots in this study are of 27-day averages of hourly averages, but because each year has 13.5 27-day periods, the 14th '27-day' average in a year is actually 14 or 15 days instead of 27 days.

We find averages (excluding 'available' 27-day averages when the specified structure was absent) of the 27-day averages that are approximately within the monthly periods for each part of the solar cycle using begin and end year and day numbers in Table 1. These SC phase averages are plotted as symbols with connecting lines for transients, HSS and slow-speed regimes in Fig. 1a. The uncertain category is not plotted in Fig. 1a, but is shown in Fig. 1b.

As previously noted, (e.g., by Richardson et al., 2000, 2002) the fraction of the solar wind occupied by transients follows the solar activity cycle. The average transient fraction of 27-day periods with transients present is 24%, whereas the average for all 'available' 27-day periods is 17%. Transients are present for ~37% of the 'available' hours in the maxima of SC 21 and SC 22, dropping to ~31% in SC 23. At solar minimum, the average occurrence frequency of transients is ~5%.

HSS from coronal holes are almost always present during each 27-day interval, and are only absent (as opposed to 'missing' where no data are available) ~4% of the time. The largest fractions of HSS are ~52% in the descent phase of the SC with the smallest fractions of ~32% in SC 21 and SC 23 solar maxima (~24% in SC 22 maximum). The slow-speed solar wind makes up the remaining solar wind structure, with the largest contribution in solar minima of ~43% (SC 20/21 and SC 23/24) to ~48% (SC 21/22 and SC 22/23), and the smallest contributions in solar maxima and the descending phases of ~30% in SCs 20 and 21 and ~35% in SCs 22 and 23.

These occurrence rates are similar to those found for solar cycles 20–23 in Richardson et al. (2002), except our solar cycle variation in the slow-speed wind is larger. The slow-speed wind and HSS are out of phase with each other in Fig. 1a because one is seen at the expense of the other.

Fig. 1b is similar to Fig. 1a except it shows the percent of hourly average auroral electron power (P_e) input that can be attributed to the different types of solar wind structures from 2 November 1978 to 2 August 2008 for hours when P_e, V_{sw}, and IMF are available (183825 h or 71% of the time). A 1 h lag time between the IMF or V_{sw} and P_e is incorporated because cross-correlations between P_e and V_{sw}, B_z, |B|, and various combinations are largest with a 1 h lag time between the IMF and V_{sw} and the resulting deposition of P_e as described in Section 3.4. We summed the average hourly P_e for each type of structure within a 27-day period, and divided by the total summed P_e during this 27-day period (including 'uncertain' structure) to derive the 27-day fractions that are plotted. The SC characteristics are similar to those in Fig. 1a, but the magnitudes are different. Thus, the contribution of transients over the entire interval increases from 17% in Fig. 1a to 23% in Fig. 1b (~35% increase), and that of HSS flows increases from 43% to 47% (~10% increase), while the contribution of the slow solar wind decreases from 37% to 27% (~30% decrease). The increase in P_e due to transients is because transients are more 'geoeffective', as explained in Section 3.2.

We find HSS contribute ~57% to P_e in the descent and minimum phases, decreasing to ~32% in solar maximum. Transients account for ~43% of P_e at solar maximum for SC 21 and SC 22, and ~38% for SC 23, with the average transient contribution dropping to ~6% in solar minimum. Slow solar wind contributes most to P_e in solar minima

Table 1
Parts of solar cycles 20–23.

SC#/#	Minimum	'27-Day' min.	Maximum	>SS#	'27-Day' max.
19/20	January 1964–October 196S	64001–6S270	December 1967–August 1970	>98	6732S–70243
20/21	April 197S–February 1977	75082–770S4	March 1979–December 1981	>138	790SS–8136S
21/22	February 198S–February 1987	8S028–870S4	December 1988–November 1991	>138	8832S–91324
22/23	May 199S–May 1997	9S109–97162	October 1999–June 2002	>103	99271–02189
23/24	February 2006–	06028–			

The solar cycle (SC) changes in solar minimum with the rise in the sunspot number, so solar minimum periods with smoothed monthly values less than 20 are shared between cycles. August 2008, the end of our study, is still in SC 23. We use the definitions of SCs 20–22 from Maris and Maris (200S), and we define solar maximum for SC 23 to include monthly smoothed sunspot numbers >103. The annual 27-day begin and end year and daynumber values used for each minimum and maximum period are also listed.

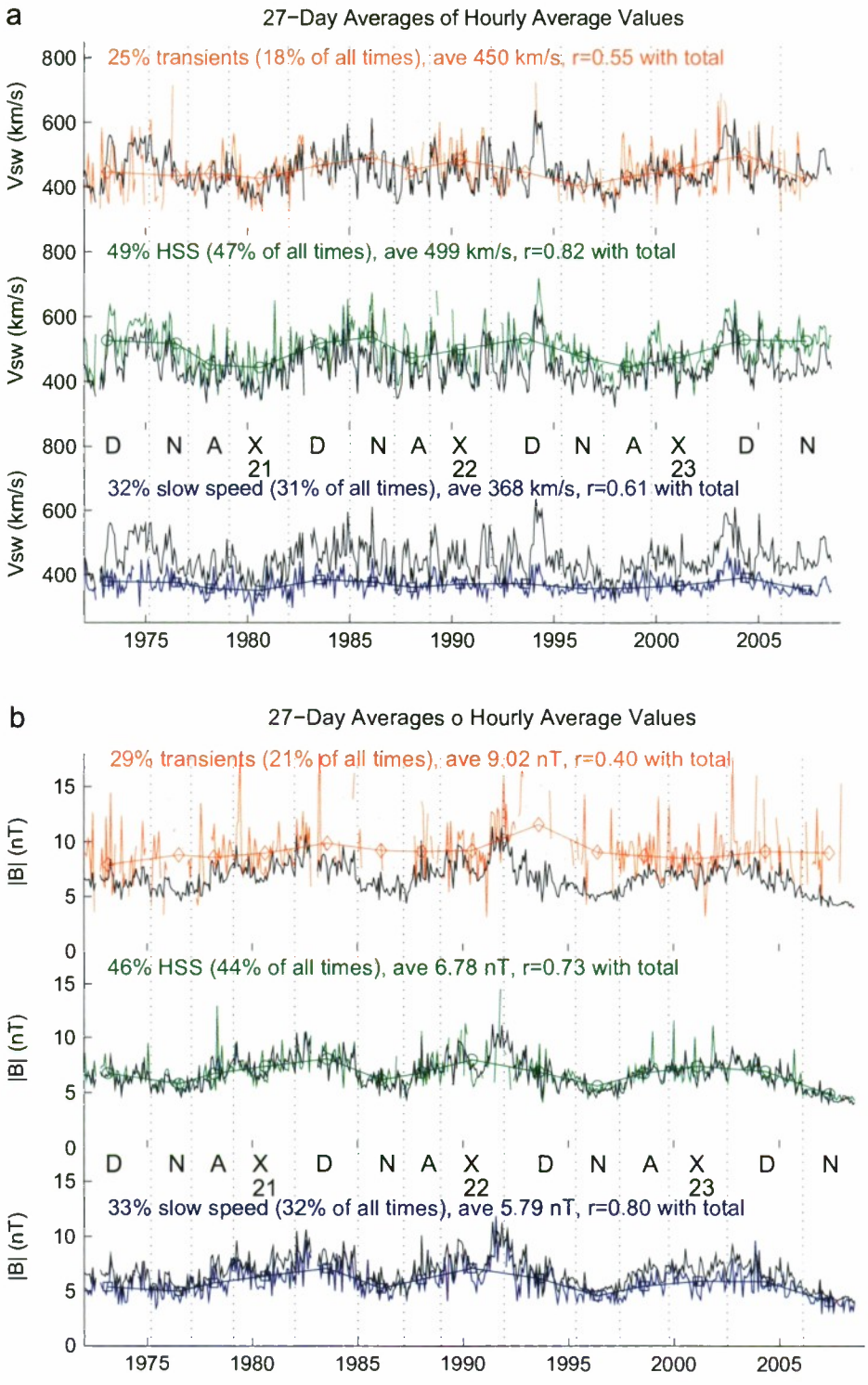

Fig. 2. (a) The average hourly solar wind speed (V_{sw}) attributed to the three types of solar wind structure plotted as 27-day averages from January 1972 to August 2008 for all days with V_{sw} and IMF, where the 'uncertain' type is not plotted. The black line is the total (including 'uncertain' but not including 'missing') V_{sw}. The average wind speeds are given for each solar wind structure, as well as the percents of the total V_{sw} with 27-day periods where the structure exists. The cross-correlation coefficient is between each structure type V_{sw} and the total V_{sw} as 27-day periods when the structure exists. The structure means in each solar cycle phase are plotted as symbols linked with straight lines. (b) Same as (a) for the average hourly scalar IMF magnitude |B|, where the black line is the total IMF magnitude. (c) Same as (a) for the average hourly incoming auroral electron power (P_e) from November 1978 where only hours with P_e, V_{sw}, and IMF are considered, where P_e lags V_{sw} and IMF by 1 h. The black line is the total P_e including those hours when V_{sw} or IMF are missing as in 1982–1983.

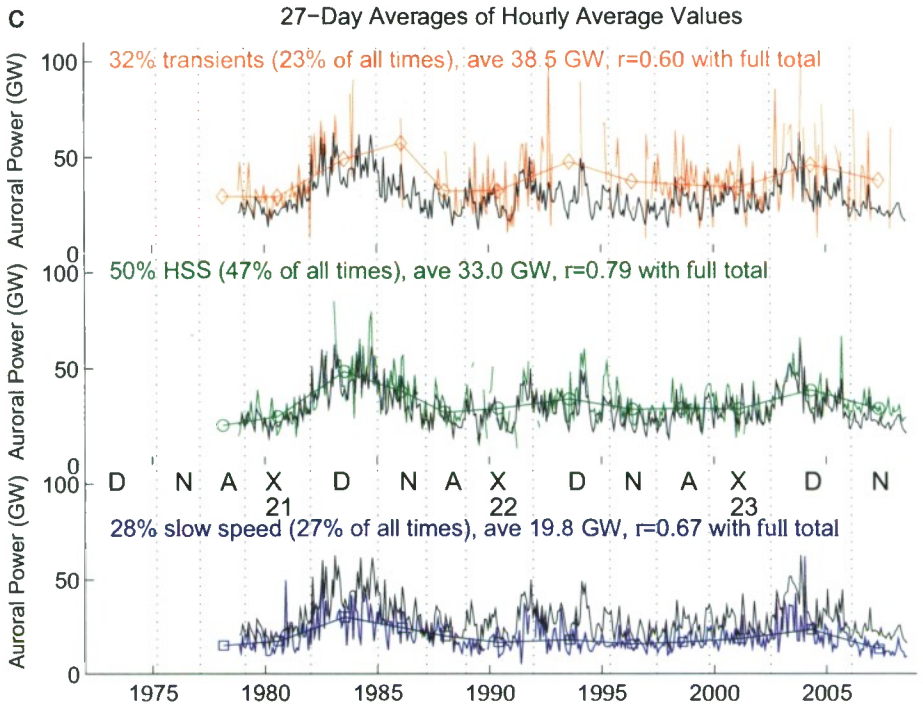

Fig. 2. (*Continued*)

(from ~27% in SC 23/24 to ~38% in SC 22/23), and ~24% in solar maxima and the descending phases.

These contributions to P_e are similar to those found by Richardson et al. (2002) for the 3-h *aa* magnetic index in SCs 20–23. They found HSS contributed ~67% to *aa* in solar minimum and ~30% at solar maximum, while transients accounted for ~50% of *aa* at solar maximum and ~10% in solar minimum. Slow solar wind contributed ~20% to *aa* throughout the solar cycle, with ~35% contribution in the SC 22/23 minimum. Mavromichalaki et al. (1988) also studied HSS and transients (as FG-HSS) with respect to the daily magnetic A_p index in terms of cross-correlations between the maximum solar wind velocity speed and A_p.

3.2. Solar cycle variations due to solar wind structure

The reason for the increased importance of transients and HSS to P_e compared with their occurrence rates is because they are associated with higher V_{sw}, and with higher IMF magnitudes than the slow-speed wind. Brautigam et al. (1991) binned DMSP electron and ion energy fluxes as a function of magnetic latitude and local time for various B_z and V_{sw} conditions. They found minimum values of HP_e for B_z ~+4 nT. HP_e increased strongly as a function of negative B_z, with only modest increases in HP_e for larger positive B_z. HP_e also doubled or tripled for V_{sw} between 346 and 572 km/s for the same negative or positive B_z values. These findings were repeated by Emery et al. (2008) using the single-pass NOAA and DMSP satellite estimates of HP_e instead of binned patterns. Liou et al. (1998) studied various MLT segments of HP_e from POLAR UV images and found IMF B_y, as well as B_z and V_{sw} variations in HP_e.

Figs. 2a and b plot the V_{sw} and IMF |B| magnitudes that are associated with the three solar wind structures from 1972 to 2008. The black lines plot the 27-day averages of the average hourly V_{sw} and |B|, while the red, green and blue lines plot the same for each solar wind structure. The average solar wind speed is highest for HSS at 499 km/s, and lowest for slow-speed winds at 368 km/s. The average V_{sw} for transients is in-between at 450 km/s. The solar wind speed for the 'uncertain' category is not plotted, but is part of the total V_{sw} in the black lines of Fig. 2a. The average total V_{sw} values are largest in the descending phase of the solar cycles in Fig. 2a because the maximum occurrence frequencies of HSS (with the largest V_{sw} values) are usually in the descending phases.

The cross-correlations are between the 27-day averages of the total V_{sw} and V_{sw} from different solar structure types. The largest cross-correlation ($r = 0.82$) is for HSS flows from coronal holes, although HSS only account for ~47% of the total V_{sw} magnitude. Thus solar wind peaks are almost always defined by HSS structures. The HSS structures are particularly prominent in Fig. 2a in the total velocity peaks around the descending phases of all solar cycles. Richardson et al. (2002) also concluded that the mean solar wind speed most closely follows variations in the speed of corotating streams (HSS). As they point out, the speeds of CME-related structures tend to converge toward that of the background solar wind (slow speed or HSS) (e.g. Lindsay et al., 1999).

We used the scalar IMF magnitude ('Bscalar' or $|B|$), rather than the vector average ('Bvector'), since the scalar average from the NASA OMNI hourly data set is composed of the average of all the IMF magnitudes in a particular hour. We found 'Bscalar' to be ~12% larger than the hourly vector average 'Bvector', which is the square root of the sum of the squares of the hourly IMF component averages. Charan Dwivedi et al. (2009) found 'Bscalar' cross-correlations with 'Bvector' to be greater than 0.90 on an hourly basis, dropping to 0.67 on a daily basis where the daily B_x, B_y and B_z values are used to find 'Bvector'.

The IMF scalar magnitude |B| in Fig. 2b shows an increase during each solar maximum. All the maxima show the bite-out in |B| around the beginning of the reversal of the magnetic field polarity (~1980, ~1990, and ~2001), which is related to the reduction in the open magnetic flux associated with the solar magnetic field polarity reversal (e.g. Richardson et al., 2000, 2002). This feature is relatively short for SCs 21 and 23 (e.g. Maris and Maris (2005) give the periods of the polarity reversals), while even solar cycles undergo longer threefold polarity reversals (Makarov and Sivaraman, 1989). The peak average values of the total |B| occur during the maximum and descending phases of the SC.

Transients carry much larger average IMF (9.02 nT) than the total average |B| because CMEs often have intrinsically strong internal fields (especially magnetic clouds). In addition, compression in the upstream sheath also increases the field strength associated with transient structures. The hourly |B| of transients does not correlate well ($r = 0.40$) with the total |B| when using 27-day averages of the hourly values. In agreement with the observations of Richardson et al. (2002), |B| for both HSS and slow-speed solar wind structures correlate well with the total |B|, although the magnitude is ~15% less in slow-speed winds.

Fig. 2c is a plot of P_e. Like V_{sw}, the total P_e values are largest in the descending phases of the solar cycle. Also like V_{sw}, P_e peaks are determined mostly by HSS periods where the cross-correlation with the total average 27-day P_e was 0.82, decreasing to 0.79 with the full total P_e including periods when the solar structure was missing. HSS sources drive the magnitude and time variation of the total P_e because HSS are present 43% of the time (from Fig. 1a), and because HSS sources result in an average P_e of 33.0 GW versus 19.8 GW from slow-speed sources (from Fig. 2c). Transients are very important during the 17% of the time they are present (from Fig. 1a), and they make up 23% of the total P_e from Fig. 2c. Transients also determine most of the storm-time variations because of their large |B| (9.02 nT from Fig. 2b), but they are absent 83% of the time. Therefore, HSS sources determine the average total magnitude of P_e, even though they represent a little less than half the solar wind source types.

There is a strong similarity of peaks in V_{sw} and peaks in P_e. The 27-day averages give cross-correlations of 0.58 for HSS V_{sw} and P_e, 0.51 for slow-speed V_{sw} and P_e, and 0.43 (not significant) for transient V_{sw} and P_e. The lack of correlation of V_{sw} and P_e for transients is probably due to the fact that the IMF B_z is more important than V_{sw} for transients in the production of P_e. Emery et al. (2008) showed that HP_e varied most with B_z negative, and secondarily HP_e varied with V_{sw} magnitude. Section 3.4 will show hourly cross-correlations between various P_e structures and solar wind parameters under negative and positive B_z conditions.

The characteristics of the average V_{sw} and average P_e are very different in each solar cycle. Maris and Maris (2005) studied the 'importance' parameter for transients (their FG-HSS) and HSS (their CH-HSS) between 1964 and 1996 (SC 20–22). The 'importance' parameter is defined as the duration of the HSS in days times the velocity gradient from the peak V_{sw} during the HSS and V_{sw} before and after the HSS. They found transients to be most important in solar maxima, with the largest values in SC 20. The importance parameters for transients in SC 21 and SC 22 were similar (as we see also in Fig. 1a), with a series of transient peaks followed by minima instead of a single increase and decrease in importance as in SC 20.

The HSS importance parameter was roughly four times more important than the transient importance parameter over their study period based on annual values in their Fig. 1. HSS importance (their CH-HSS) was largest in the descending part of the SC, and was least in the maxima. From Fig. 1a, we also see HSS are most important in the descending phases and least important in the maxima in terms of the occurrence frequency. Maris and Maris (2005) found the largest HSS importance values between SC 20/21 minimum and the descent phase of SC 21. From Figs 1a and 2a, we find the occurrence frequency of HSS and the magnitude of V_{sw} to be about the same for SC 21 as for the other cycles. Maris and Maris (2005) found HSS in SC 20 and SC 22 to be similar in the ascent and maxima phases. They suggested with Mavromichalaki et al. (1999) that the 22-year magnetic cycle imprints different features in the occurrence rate of the HSS in the ascendant and descendant phases of the odd and even cycles. We will discuss the 22-year magnetic cycle in terms of V_{sw} from Figs 1a and 2a.

3.3. 22-Year Hale cycle variations in solar wind and auroral electron power

Cliver et al. (1996) showed that the 22-year cycle in geomagnetic *aa* activity is characterized by high activity during the second half (descending and minimum phases) of even-numbered solar cycles and the first half (ascending and maximum phases) of odd-numbered cycles, or *aa* is strongest in the middle of each 22-year Hale cycle. We anticipate that this increased magnitude may also be found in P_e because of the close correspondence of P_e with 3-h K_p and a_p (Emery et al., 2008). Russell and McPherron (1973) argued that because of the 7° tilt of the solar equator to the ecliptic as manifested in the Rosenberg and Coleman (1969) effect, the excess positive GSE B_y in the fall and excess negative GSE B_y in the spring results in an excess negative GSM B_z component that produces more magnetic activity on Earth in the middle of each Hale cycle. Cliver et al. (1996) acknowledged the combined Russell–McPherron and Rosenberg–Coleman geometrical effects, but they reminded the community that there is an

additional intrinsic solar Hale cycle. The Hale cycle shows higher sunspot numbers in the second half of even-numbered SCs and in the first half of odd-numbered SCs, where the maximum sunspot numbers are found in the odd SC maximum. They proposed a relative excess of HSS in the descent and minimum of even SCs in conjuction with stronger solar poloidal magnetic fields, and a relative excess of transients during the rise and maximum of odd SCs. Since the Hale cycle was reversed in SCs 22–23, where the highest sunspot numbers were in the even SC 22 instead of in the odd SC 23, we might expect to find a relative excess of HSS in the descent and minimum of SC 23 instead of in the descent and minimum of SC 22.

From Fig. 1a, we see that the occurrence frequencies of HSS in the descending and minimum phases of SC 20 are larger than in SC 21, in agreement with the hypothesis of Cliver et al. (1996), although the HSS and total V_{sw} magnitudes are similar. For the unusual Hale 22–23 cycle, the HSS V_{sw} occurrence frequencies and magnitudes in D22 and D23 are similar, but the HSS occurrence frequency in the incomplete N23/24 phase is slightly larger than in D23, and is 8% larger than in N22/23. In addition, the HSS and total V_{sw} magnitudes for N23/24 are 11% and 8% larger, respectively, than in N22/23. In Fig. 1b, the fraction of P_e deposited by HSS is exceptionally high in the descending phase of SC 22, but the fraction of P_e deposited by HSS is highest in the minimum phase of SC 23/24 compared with the 22/23 minimum. The magnitudes of HSS and total P_e are ~15% higher in D23 compared to D22, but are approximately the same in N22/23 and N23/24. From Fig. 2b, the total IMF magnitude is about the same in D22 and D23, but is ~14% smaller in N23/24 compared to N22/23. Since the magnitude of P_e is influenced by IMF as well as V_{sw}, the decrease in IMF balances the increase in V_{sw} in N23/24 compared to N22/23 in the resulting magnitude of P_e. The increased occurrence frequencies of HSS in P_e and V_{sw} in N23/24 compared with N22/23 is opposite to the normal Hale cycle, but fits with the abnormal 22–23 Hale cycle.

When we examine the ascending parts of the solar cycle, we see from Fig. 1a that transients account for ~25% of the solar wind structures in SCs 21 and 23, but only ~11% of all times in SC 22, in agreement with the hypothesis of a relative excess of transients in the ascending phases of odd SCs. This relative excess of transients is also seen in the fraction of P_e deposited by transients in Fig. 1b. However, the occurrence frequency of transients is largest in the even SC 22 maximum compared with the odd SCs 21 and 23, which is consistent with an abnormal 22–23 Hale cycle. The results of the last three solar cycles are mixed with respect to regular Hale cycles in P_e due to changing ratios of HSS and transients, partly because of the unusual 22–23 Hale cycle.

3.4. Cross-correlation of V_{sw}, IMF, and P_e for different solar wind structures

Similar to the cross-correlations found for the southern hemisphere HP_e by Emery et al. (2008), the highest cross-correlations for hourly P_e between 1978 and 2008 are with 3-h K_p and a_p at 0.72 and 0.68, respectively, (0.90 and 0.84 for daily P_e). Thus, we anticipate that cross-correlations of P_e with V_{sw} and IMF will be similar to cross-correlations with daily A_p. Charan Dwivedi et al. (2009) have reviewed the literature of cross-correlations of interplanetary plasma and fields with daily or longer A_p values. Crooker et al. (1977) found 6-month and yearly averages of A_p to be highly correlated with V_{sw}^2 ($r = 0.86$), $V_{sw}B_s$ ($r = 0.8$), or $V_{sw}^2B_s$ ($r = 0.9$), where B_s is the southward component of B_z, or B_z negative. Ahluwalia (2000) focused on the IMF magnitude $|B|$ instead of B_s, and found good correlations ($r = 0.92$) with $V_{sw}|B|$ and $V_{sw}^2|B|$ for annual averages. Charan Dwivedi et al. (2009) found cross-correlations of daily A_p with $V_{sw}|B|$ to vary between 0.61 in 1985 to 0.86 in 1986 and 2001 from their Fig. 4, with relatively low cross-correlations for even SC ascending phases and relatively high cross-correlations for odd SC ascending phases.

Recently, Lei et al. (2008b) found 11-day running means of the neutral thermospheric density at 400 km to correlate with K_p with cross-correlations increasing from 0.78 to 0.96 between 2002 and 2007 from their Fig. 2. In the same figure, they found cross-correlations with $\log(V_{sw}^2|B|)$ to increase from 0.71 to 0.92 in the same time period. The neutral density is affected by Joule heating in high latitudes caused by increased conductance from particle precipitation (P_e) and by electric fields (ion drifts) imposed from the magnetosphere, which are particularly high during B_z negative periods.

We calculated the daily and hourly cross-correlations between P_e and V_{sw}, B_z, $|B|$, $V_{sw}B_z$, $V_{sw}B_{yz}$, $V_{sw}|B|$, $V_{sw}^2B_z$, $V_{sw}^2|B|$, $V_{sw}|B|^2$, $\log(V_{sw}|B|)$, $\log(V_{sw}^2|B|)$, and $\log(V_{sw}|B|^2)$, where B_{yz} is the vector average of B_y and B_z, or the square root of the sum of the squares of their hourly averages. For hourly data, the best correlations between P_e and most of the solar wind parameters occurred when P_e lagged the solar wind parameters by 1 h. Cross-correlations were found for B_z negative, $B_z >= 0$, and all B_z conditions, for each type of solar wind structure for 1978–2008 where all parameters were available. All cross-correlations were significant (>0.5) for at least one type of solar wind structure for B_z negative or positive conditions. Usually, hourly cross-correlations were less than daily cross-correlations by ~0.20 for $V_{sw}|B|$ combinations, ~0.15 for V_{sw} or $|B|$ alone, less than 0.10 for B_z combinations, and about the same for B_z alone. The cross-correlations were larger for the combination of the HSS and slow-speed solar wind, rather than for HSS or slow-speed winds alone for V_{sw} or combinations with V_{sw} and $|B|$ or B_{yz}.

HP_e increases strongly with increasing B_z negative values and with increasing V_{sw} magnitudes (Brautigam et al., 1991; Liou et al., 1998; Emery et al., 2008), so correlations of P_e with B_z and V_{sw} were examined first as a function of solar wind structure. Transients and the slow-speed wind P_e correlated well with hourly B_z for B_z negative conditions with cross-correlation coefficients of −0.63 and −0.64, respectively, while HSS P_e cross-correlations were −0.51. Thus B_z negative is more effective in producing P_e during transient or slow-speed wind conditions than during HSS. However, HSS and slow-speed wind P_e cross-correlations with hourly V_{sw} were 0.54

compared to transient P_e cross-correlations of 0.45, showing that V_{sw} is relatively more effective for HSS conditions compared to transient conditions. The correlation of P_e with V_{sw} for positive B_z conditions is expected because previous studies found HP_e increases only slowly with increasing B_z positive while HP_e doubles between V_{sw} of 300 and 600 km/s (Brautigam et al., 1991; Emery et al., 2008). Cross-correlations of P_e were usually insignificant (<0.5) for B_z positive conditions for any combination with B_z. However, daily cross-correlations of P_e with $|B|$ during transient or slow-speed wind conditions were just over 0.50, and $V_{sw}B_{xy}$ daily cross-correlations with P_e were also significant for B_z positive and especially B_z negative conditions.

The best overall cross-correlations of hourly P_e (lagged 1 h) and daily P_e for B_z positive and negative conditions were found for $\log(V_{sw}^2|B|)$, $V_{sw}^2|B|$, and $V_{sw}|B|$. The range of hourly cross-correlations of P_e with these combinations are 0.56–0.61, 0.50–0.60, and 0.56–0.62, respectively for B_z negative conditions and 0.49–0.57, 0.47–0.60, and 0.47–0.53, respectively for B_z positive conditions, where the lower numbers are during transient solar wind conditions and the higher numbers are for the combination of HSS and slow-speed wind. $V_{sw}^2B_z$ is expected from theoretical considerations to be a better choice for a power input like P_e (e.g. Table 2 of Gonzalez et al., 1994) because it it is part of the merging energy transfer term at the magnetopause. However, the interplanetary electric field $V_{sw}|B|$ also correlates well with P_e as with A_p. $|B|$ combinations in particular correlate well for HSS because the geomagnetic disturbances are caused by the southward component of large-amplitude Alfven waves in the solar wind (Tsurutani et al., 1995), and so the fluctuations in the IMF and thus $|B|$ are more important for HSS compared to the relatively slow variations in IMF experienced in transient solar structures.

Fig. 3a and b show the daily average $V_{sw}|B|$ values in mV/m against the daily average P_e values between 1978 and 2008 for B_z negative and positive conditions. The daily (solid line) and hourly (dashed line) fits are also plotted, where the HSS and slow-speed wind fits are linear and the transient fits are quadratic. The P_e values are larger for B_z negative conditions, as expected, where the largest $V_{sw}|B|$ values are during transients with large $|B|$ values as shown in Fig. 2b. Usually the largest P_e values are brought by transient solar wind structures, although HSS in B_z positive conditions can precipitate relatively large P_e. The hourly fits are for larger values of P_e than the daily fits for B_z negative conditions, while the hourly fits are for smaller values of P_e for B_z positive conditions. This shows that an equivalent increase in the IMF magnitude (or B_z) results in larger P_e for B_z negative conditions and not much increase in P_e for B_z positive conditions, as expected.

For B_z positive conditions, the lower P_e values are during transient solar wind structures, showing that $|B|$ increases are not as effective for P_e during transient structures compared to HSS structures. For B_z negative conditions, the difference between the P_e during transient structures is a little higher compared to slow-speed and HSS structures for interplanetary electric fields less than 6 mV/m, indicating that the same $|B|$ (or B_z) is more

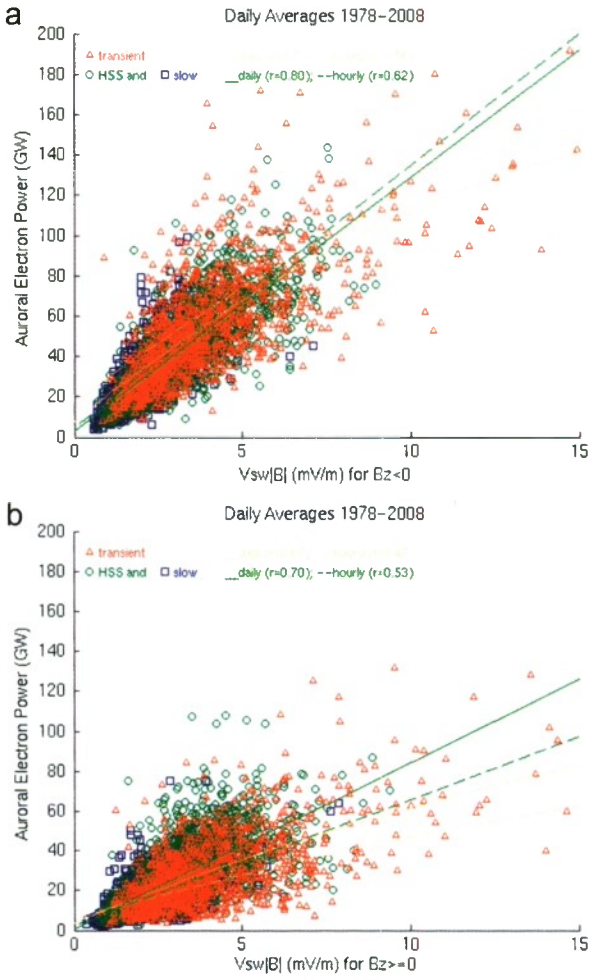

Fig. 3. (a) The daily averages of the hourly products of solar wind speed (V_{sw}) and scalar IMF $|B|$ in three types of daily solar wind structures versus the daily average auroral electron power (P_e) for average daily IMF B_z negative conditions from November 1978 to August 2008 for all hours with V_{sw}, IMF, and P_e. P_e lags V_{sw} and IMF by 1 h. The green lines are linear fits for HSS combined with slow-speed winds for the plotted daily averages (solid) and for the hourly fit (dashed). The orange lines are quadratic fits of P_e to $V_{sw}|B|$ for daily (solid) and hourly (dashed) averages with transient solar structures. The corresponding daily and hourly cross-correlations are also listed. (b) Same as (a) for B_z positive conditions.

effective in depositing larger P_e for transients, probably because the B_z negative conditions last longer. The difference in transient P_e magnitudes compared to HSS P_e magnitudes as a function of the sign of B_z emphasizes the different characteristics of transients compared to HSS.

For B_z negative conditions, slightly better cross-correlations with hourly P_e were found with $V_{sw}^2B_z$ ($r=-0.64$) and $V_{sw}B_z$ ($r=-0.62$) for HSS and slow-speed wind conditions, and much better cross-correlations were found with $V_{sw}B_z$ ($r=-0.65$), B_z ($r=-0.63$), $V_{sw}^2B_z$ ($r=-0.60$), and $V_{sw}B_{yz}$ ($r=0.58$) during hours with transient solar structures. These are similar to the hourly cross-correlations of $V_{sw}B_z$ and $V_{sw}^2B_z$ with HPe in the southern hemisphere found in Emery et al. (2008).

Because P_e is larger for B_z negative conditions than for B_z positive conditions, the cross-correlations of hourly P_e with all B_z conditions is often worse than the cross-correlations for either B_z condition because of the increased scatter in the P_e values. B_z positive cross-correlations for P_e are largest for HSS structures compared to transient structures, while B_z negative cross-correlations are similar for combinations including B_z.

Charan Dwivedi et al. (2009) found cross-correlations of daily A_p with $V_{sw}|B|$ to be relatively small in even SC ascending phases (~0.70 in A20 and ~0.65 in A22) and relatively large in odd SC ascending phases (~0.75 in A21 and ~0.80 in A23). We found the cross-correlations of daily P_e with $V_{sw}|B|$ were 0.56 in 1987–1988 (~A22), and were 0.73 in 1997–1998 (~A23), for all B_z and solar wind structure conditions. The transient cross-correlations of P_e with $V_{sw}|B|$ were 0.07 worse than those for HSS and slow-speed winds in A22, and better than them by 0.05 in A23 when the percentage of transients nearly doubled. However, part of the reason for the poor correlations in 1987–1988 could be that the solar wind plasma or IMF observations were missing on 33% of the days.

4. Periodic analyses of solar wind and auroral electron power

4.1. Lomb–Scargle analyses

Several authors have analyzed the spectral characteristics of the solar wind. Svalgaard and Wilcox (1975) studied the IMF B_x periodicity over five solar cycles and found a strong 27-day periodicity. Gosling et al. (1976, 1977) reported 27-day periodicities in V_{sw}, with peaks at 13.5 days for certain years, and weak or absent 7-day periodicities. Similarly, several authors found 27-, 13.5-day (one half of 27-day), 9-day (one third of 27-day) and 7-day (one fourth of 27-day) periodicities in the IMF and V_{sw} (Neugebauer et al., 2000; Nayar et al., 2001; Verma, 2001; Temmer et al., 2007). Mursula and Zieger (1996) showed the 27- and 13.5-day periodicities in V_{sw}, IMF sector component and K_p, and ascribed the 13.5-day periodicity to the occurrence at 1 AU of two HSS per solar rotation corresponding to two different magnetic polarity sectors with a tilted heliosheet. Lindblad (1981) showed a preference for HSS on Bartels day 17 for B_x negative (toward the Sun), and a preference for Bartels day 4 for B_x positive (away from the Sun), corresponding to two HSS per solar rotation. Rangarajan and Mavromichalaki (1989) found similar preferences for HSS, with additional preferences for transients on Bartels days 11 and 25 for B_x negative and positive sectors.

Because of the high correlations of P_e and HP_e with 3-h K_p and a_p (Section 3.4 and Emery et al., 2008), we anticipate similar periodicities in geomagnetic indices and P_e. The major periodicities of the Earth's geomagnetic indices K_p, A_p, or aa are for 11.1-year, 17.5, 12.7, and 6 months, with shorter 27- and 13.5-day periods (e.g. Delouis and Mayaud, 1975; Gonzalez et al., 1990; Gorney, 1990; Prestes et al., 2006). The 22-year Hale cycle is seen in some studies, and not seen in others (Prestes et al., 2006). The 6-month periodicity is quite marked, especially after 1930 when the solar variability increased during solar minima (Prestes et al., 2006). Cliver et al. (2000) attributed ~65% of this semiannual variation to the equinoctial effect based on the angle between the solar wind flow direction and the Earth's dipole axis that makes the IMF coupling ~25% less effective at the solstices. The remaining 6-month periodicity was attributed ~20% to the axial effect and ~15% to the Russell–McPherron effect (Russell and McPherron, 1973). The axial effect reflects changes in the solar wind parameters measured at 1 AU because the Earth is at the highest heliospheric latitudes on 6 March (−7.2°) and on 6 September (+7.2°) (e.g. Cliver et al., 1996), where it is more in line with solar midlatitude coronal holes (e.g. Bohlin, 1977). Cliver et al. (2000) found a 6 km/s semiannual variation in V_{sw} from 1963 to 1997 on a background average V_{sw} of ~440 km/s.

From the previous sections, we anticipate that some of the periodicities in V_{sw} will be in P_e. We also anticipate finding an enhanced semiannual periodicity (~183 days) similar to that found in the K_p index for P_e, which maximizes in the equinoxes when magnetospheric reconnection is increased compared with solstices (e.g. Cliver et al., 2000).

We used a Lomb–Scargle analysis (Lomb, 1976; Scargle, 1982) of hourly total V_{sw} and P_e because a Lomb analysis can handle the significant gaps in V_{sw} data before about 1995 (the launch of the WIND spacecraft). The full P_e data were used, since there were very few data gaps. Several authors have used and discussed the advantages of the Lomb analysis over the traditional fast Fourier transform (FFT) method or other methods (e.g. Harrington et al., 1996; Vityazev, 1997; Laguna et al., 1998; Thong et al., 2004). Thong et al. (2004) averaged different Lomb–Scargle transforms after de-normalization of the Lomb transform, which is variance (σ^2) normalized in spectral power y. The spectral power y is converted to amplitude A as $A = 2\sqrt{(y\sigma^2/N)}$, where N is the number of sample points.

We want to compare the hourly V_{sw} and P_e amplitudes at several periodicities over several solar cycles. To test our Lomb–Scargle analyses, we calculated FFT amplitudes using daily V_{sw} and P_e values for each year of data where data gaps were filled in. The amplitudes and periods from both Lomb–Scargle and FFT analyses were similar, although the Lomb analyses had better frequency resolution. The Lomb results were also similar using hourly values in place of daily values. Thus, the following Lomb–Scargle periodic analyses use hourly V_{sw} and P_e over various time intervals.

We are interested in the periodicities and in the maximum amplitudes of these periodicities. Figs 4a–d show the Lomb analysis of the hourly V_{sw} and P_e in the descending phase of SC 23 from 02190 to 06027 when HSS were present for 50% of the time, with transients present 16% of the time and slow-speed wind the remaining 34% of the time, as shown in Fig. 1a. Fig. 4a shows the total V_{sw} and P_e, while Fig. 4b is only for the hours with transients, Fig. 4c for the HSS hours, and Fig. 4d for the slow-speed hours. As anticipated, the transient periodicities in Fig. 4b

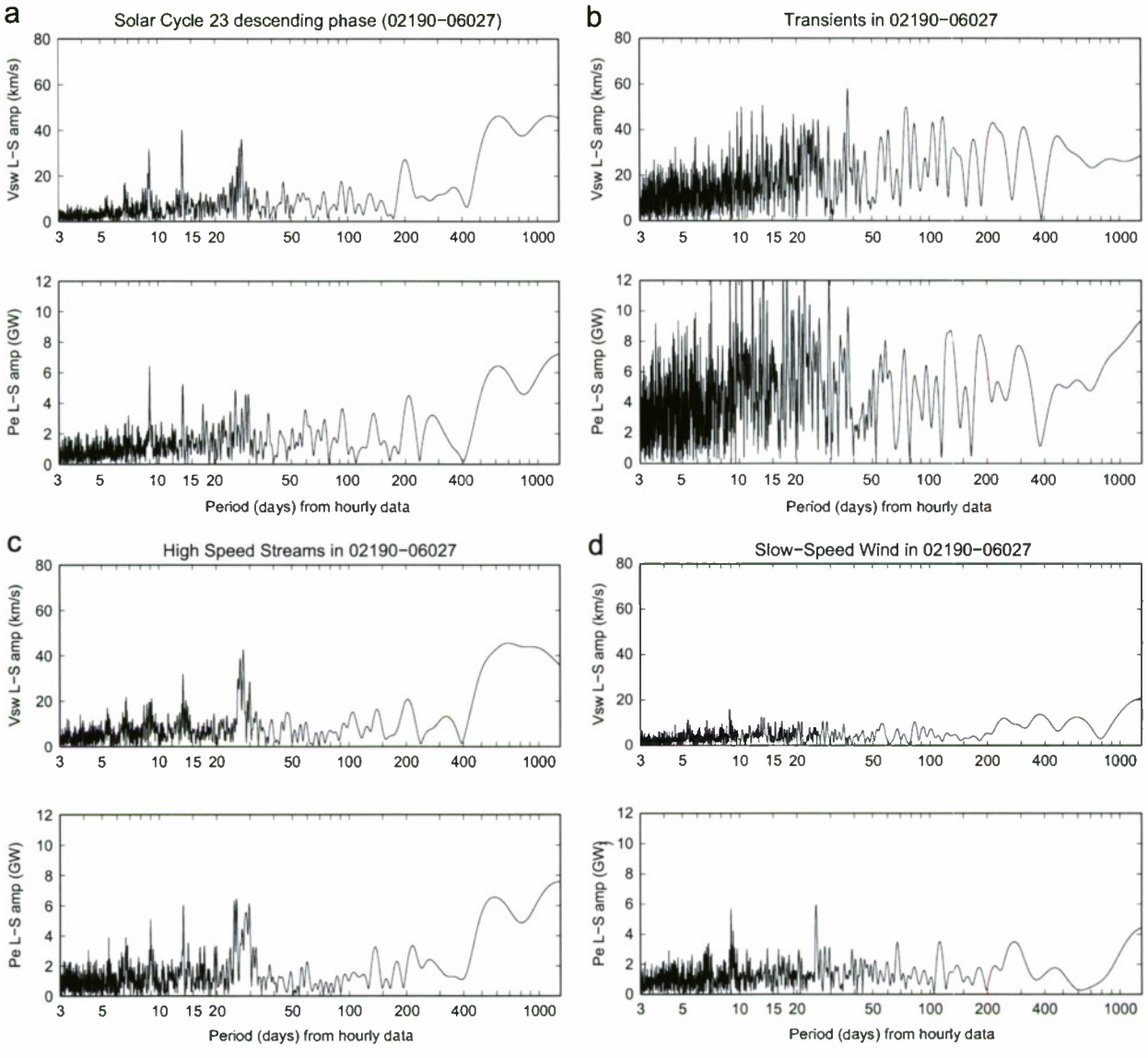

Fig. 4. (a) Lomb-Scargle spectral amplitudes using all the hourly V_{sw} and P_e values during SC 23 descending phase (02190–06027). (b) Same as (a) for all hours with transients. (c) Same as (a) for all hours with HSS. (d) Same as (a) for all hours with slow speed wind.

are much noisier than any of the other solar structures. The periodicities around 5, 7, 9, 13.5, and 27 days seen in all V_{sw} and P_e data in Fig. 4a are clearest in Fig. 4c for HSS hours, suggesting that HSS structures impose the most structure on V_{sw} and P_e. These periodicities are also seen in |B|, B_x, and GSM B_y, but are not evident in GSM B_z (not shown). For B_x and B_y, there are strong amplitudes of 13.5 and 27 days reflecting the sector structure of a tilted heliosheet (e.g. Mursula and Zieger, 1996). The HSS and total spectra are especially close for V_{sw}, while for P_e, 7-, 9- and 25-day peaks are also relatively large in the slow-speed wind. The P_e peak at ~208 days in Fig. 4a appears to be shifted from 'semiannual' (~183 days) peaks in the HSS and slow-speed hours in Figs. 4c and d by the significant amplitudes ~200 days seen in the transient hours in Fig. 4b.

We made similar analyses for other solar cycle phase intervals indicated in Table 1. In general, the 7-, 9-, 13.5-, 25-, 27-, and 29-day periodicities in V_{sw} usually also appear in P_e. The longer periodicities are sometimes in both, and sometimes are not. Figs. 5a and b are the periodicities for the total V_{sw} and P_e for 366 days in the SC 22/23 minimum from 96031 to 97030, and in the SC 23/24 minimum from 07209 to 08209, respectively. Gibson et al. (2009) discuss these solar minimum periodicities in the context of the solar drivers and their effects on the whole geospace system. Both solar minima show periodicities in the total V_{sw} and P_e around 27, 13.5, 9, 7 and 5 days, but the amplitudes in SC 23/24 are much stronger and cleaner. In SC minimum 22/23, there is also a very strong 'semiannual' peak in both V_{sw} and P_e. We will discuss the differences in these strong solar minimum amplitudes in Section 4.3.

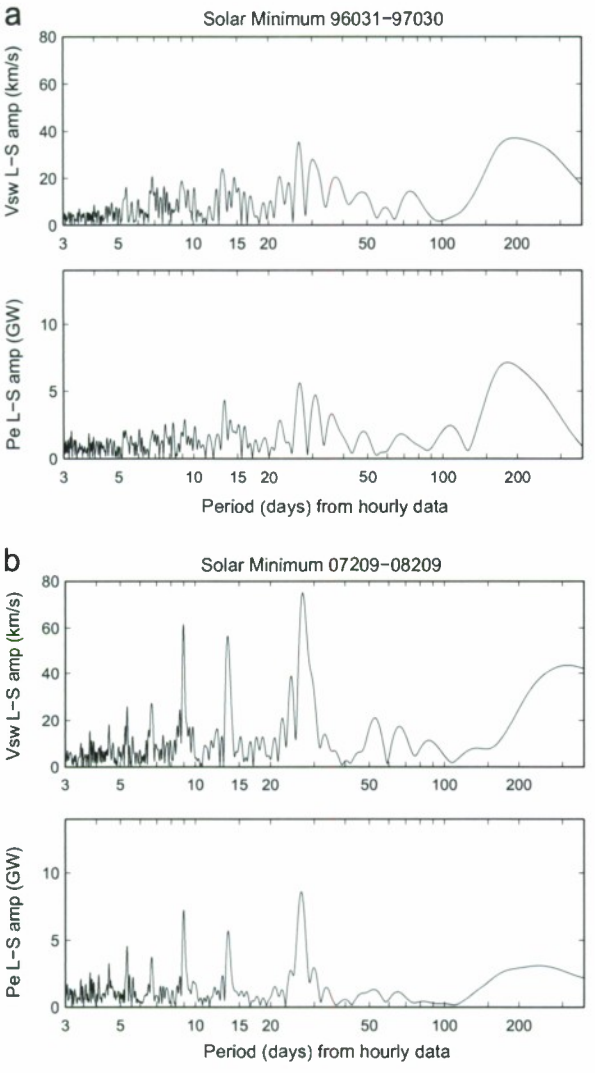

Fig. 5. (a) Lomb-Scargle spectral amplitudes using all the hourly V_{sw} and P_e values in one year during SC 22/23 minimum (96031–97030). (b) Same as (a) for one year during SC 23/24 minimum (07209–08209).

4.2. Solar rotation periodicities

Fig. 6a shows the Lomb amplitudes for the total hourly V_{sw} as red triangles and P_e as dark green x's in the solar rotation and related periodicities of 7-, 9-, 13.5-, 27-day, and the maximum of the 25- and 29-day amplitudes. These periodicities are almost always present in V_{sw} and in P_e, and are correlated. The Lomb amplitudes using hourly V_{sw} and P_e values over yearly intervals are plotted as magenta diamonds and cyan circles. The y-axes are in km/s (V_{sw}) and GW (P_e), where a dotted line is drawn at 5 GW (~33.8 km/s) as guidance.

Cliver et al. (1996) studied the daily and longer *aa* index using fast Fourier transform (FFT) analyses for six Hale cycles from 1844 to 1994. They found the *aa* activity to be enhanced in the descending and minimum (DN) even cycles and in the ascending and maximum (AX) odd cycles in the middle of each Hale cycle. They showed that the 182-, 27-, and 13.5-day amplitudes were largest for DN even cycles, with 9-day amplitudes about the same for DN even and odd cycles. They suggested, that in addition to the enhanced GSM B_z negative from the Russell-McPherron and Rosenberg–Coleman effects, that faster and longer duration HSS in DN even cycles accounted for the DN increases in *aa*, and that CMEs in AX odd cycles produced the *aa* increases in odd AX cycles. Cliver et al. (1996) also found that the adjacent 25- and 29-day periodicities in *aa* were larger and more common for DN even cycles. Again, because the 22–23 Hale cycle is unusual, these findings may not hold for in this Hale cycle.

The 'importance' parameter of Maris and Maris (2005) was highest for DN20 followed by DN21 for HSS, which confirms the Cliver et al. (1996) results of more active HSS in DN even cycles. But for transients, the 'importance' parameter in Maris and Maris (2005) was highest in AX20, followed by AX22 and finally by AX21, which is against the Cliver et al. (1996) speculation that transients contribute most in AX phases of odd cycles.

From our study, we see in Fig. 6a that the 27-day and the maximum of the subsidiary 25- and 29-day periodicities are relatively strong for V_{sw} and P_e in all DN cycles, especially in the yearly amplitudes, which is different from the *aa* index findings of Cliver et al. (1996). Similarly, the 7-, 9- and 13.5-day periodicities are strongest in all DN phases. The strongest 13.5-day periodicity in V_{sw} is during DN20 in agreement with Cliver et al. (1996).

We also see in Fig. 6a strong 9-day periodicities in V_{sw} and P_e during DN23, especially in 2005. This is in agreement with the observations of Temmer et al. (2007), who found the 9-day period in 2005 was caused by three CHs distributed ~120° apart in solar longitude. Mlynczak et al. (2008) found a similar 9-day periodicity in the infrared cooling from 2002 to 2006 by [NO] and [CO_2] between 100 and 200 km. They found a 9-day periodicity in daily A_p and K_p, but did not find any 9-day periodicity in the solar ultraviolet (UV) data. Lei et al. (2008a,b) and Thayer et al. (2008) also found 9- and 7-day periodicities in the neutral density ~400 km from the CHAMP satellite between 2004 and 2007. The 7- and 9-day periodicities in V_{sw} and P_e were also strong for DN23 as shown in Figs. 4a, 5b, and 6a. In Figs. 2a and c, we see exceptionally large contributions from HSS to the total V_{sw} and P_e in N23/24. There are correspondingly lower contributions to the total V_{sw} and P_e by the slow solar wind.

4.3. Semiannual and other longer periodicities

In Fig. 6b, we plot Lomb amplitudes in km/s and GW of periodicities longer than 100 days in the hourly V_{sw} and P_e during SC phases and yearly intervals. The yearly amplitudes are shown in the top panel. The longest periodicity shown is for the 1.3–1.4 year (465–520 days or 15.2–17.1 months) periodicity in the Sun that was observed in the solar wind starting in 1987 by Richardson et al. (1994). In Fig. 6b, we see it relatively strong in V_{sw} and P_e for SC 22, but not always in the same phases. Prestes et al. (2006) have a relatively strong periodicity in monthly *aa* and A_p at 15.9 and 16.9 months in their Fig. 5.

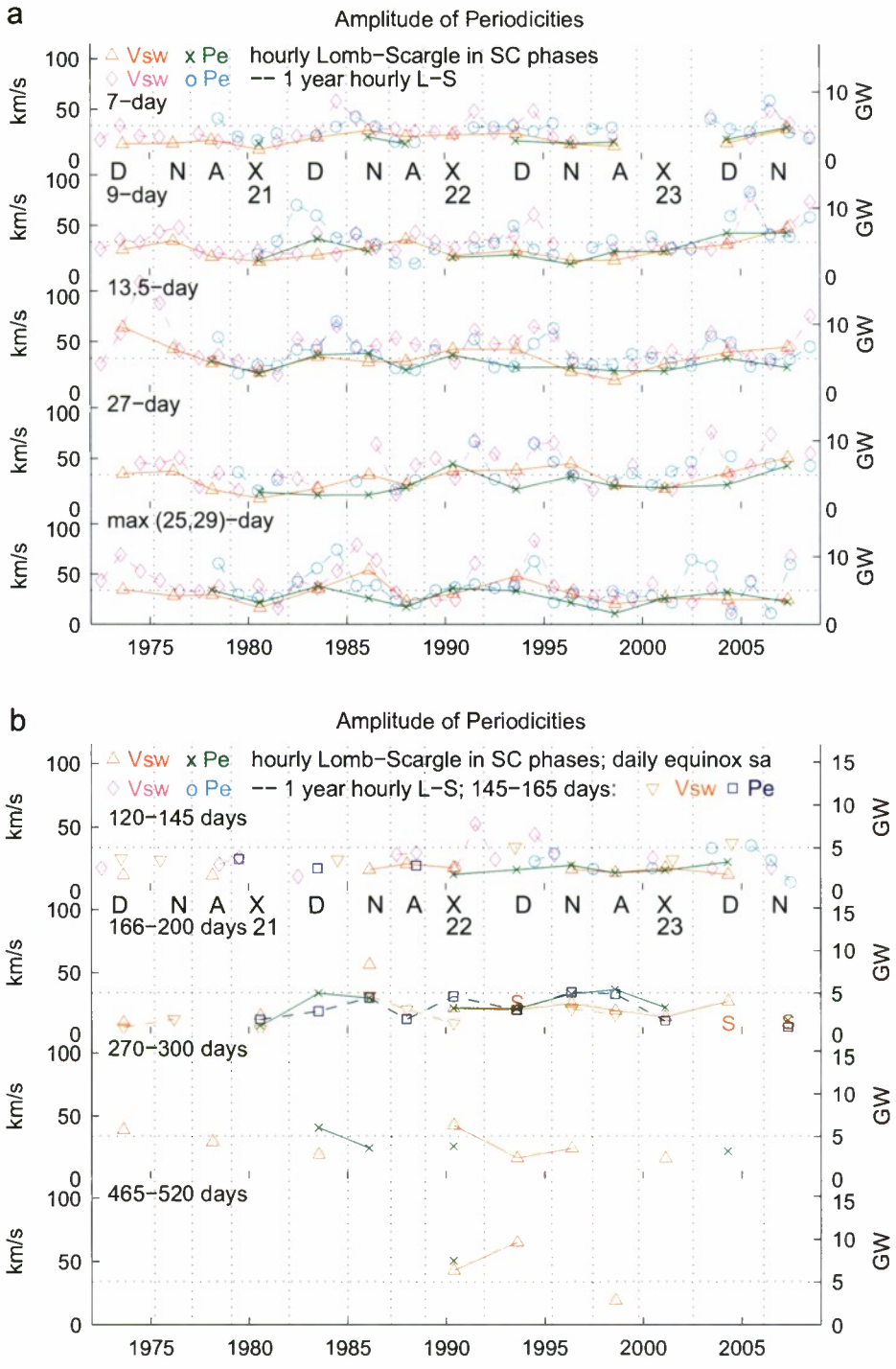

Fig. 6. (a) Amplitudes from the Lomb-Scargle analyses of all hourly P_e (as green x's) and all hourly V_{sw} (as red triangles) for 7-, 9-, 13.5-, 27-day, and the maximum of 25 or 29-day periods related to the solar rotation period over the descending (D), minimum (N), ascending (A) and maximum (X) phases of the solar cycle. Yearly Lomb-Scargle amplitudes of V_{sw} are magenta diamonds and are cyan circles for P_e at the midpoint of each year. (b) Same as (a) for periods of 120–145 days, 166–200 days (semiannual), 270–300 days, and 465–520 days (1.3–1.4 years) from the hourly Lomb-Scargle analyses. Yearly Lomb-Scargle amplitudes as diamonds (V_{sw}) and circles (P_e) are dashed lines in the top panel. Yearly Lomb-Scargle amplitudes between 145 and 165 days are shown as inverted triangles (V_{sw}) and squares (P_e) in the plot for 120–145 days. These same symbols are used with dashed lines in the second panel for equinox semiannual (sa) amplitudes from polynomial fits to daily V_{sw} and P_e data sorted by daynumber. Solstice semiannual amplitudes in V_{sw} are marked with 'S'.

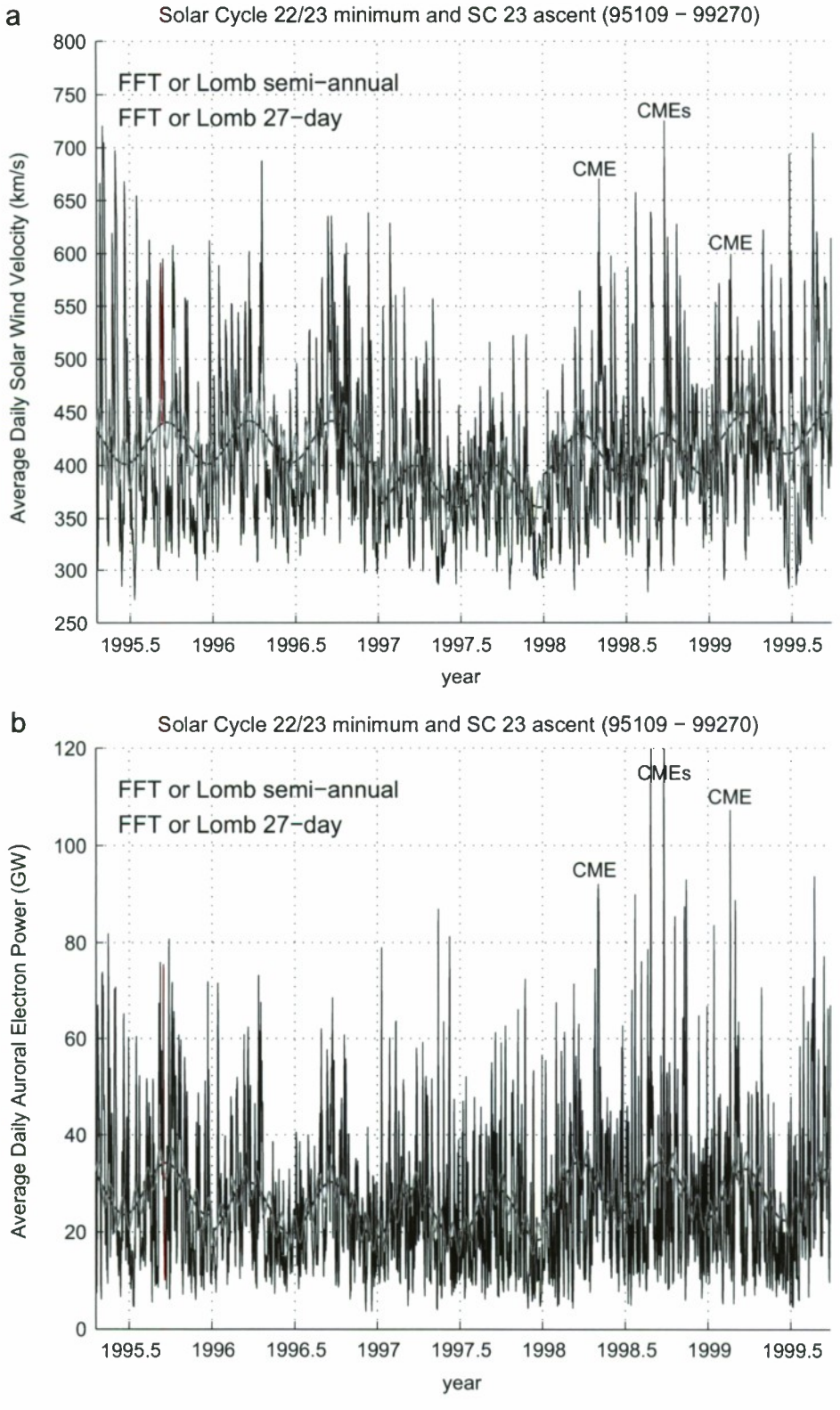

Fig. 7. (a) Average daily solar wind velocity from 95109 to 99270 (SC 22/23 minimum and SC 23 ascending phase) showing the averages of the FFT and Lomb-Scargle semiannual fits in blue, and the 27-day fits in magenta on top of annual averages, with several CMEs labeled. (b) Same as (a) for the daily average auroral electron power.

Silverman and Shapiro (1983) showed this 1.4-year periodicity in auroral sightings in Sweden from 1721 to 1943, with peaks approximately every 65–68 years (~1764, ~1832, ~1878, and by extrapolation ~1948 and ~2013). The reason for this 1.3–1.4-year variability is not known.

The periodicity for 270–300 days (8.9–9.9 months) plotted in the third panel of Fig. 6b is relatively common in the hourly V_{sw}, with significant amplitudes at times. This periodicity is only weakly present in P_e. Prestes et al. (2006) show a ~9.1-month periodicity in monthly *aa* and A_p in their Fig. 5.

Richardson and Cane (2005) described an intermittent ~150-day quasi-periodicity in interplanetary and solar phenomena during SC 23. Lean (1990) noted that it usually appeared around the maxima of cycles 12–21 in sunspot areas with a period between 130 and 185 days. We split this ~150-day periodicity into three sections between 120 and 145 days (3.9–4.8 months) and the semiannual periodicity between 166 and 200 days (5.5–6.6 months), with the intervening periodicity of 145–165 days (4.8–5.5 months) plotted as inverted triangles (V_{sw}) and squares (P_e) on the 145–165 day plot in Fig. 6b in the top panel. Periodicities in V_{sw} and P_e between 120–145 days and 145–165 days are relatively weak compared with the solar rotation periodicities in Fig. 6a. These periodicities were listed by Prestes et al. (2006) for monthly *aa* and A_p from 1932 to 2001 as 4.7 and 4.9 months (143 and 149 days).

The 'semiannual' amplitudes are shown in the second panel of Fig. 6b. The largest 'semiannual' Lomb power in V_{sw} is for N21/22 at 56 km/s for 189 days. The largest P_e amplitudes are yearly peaks in 1982 at 174 days, in 1996 at 193 days, and in 1999 at 192 days. The 'semiannual' peaks in V_{sw} and P_e during 96031–97030 are also shown in Fig. 5a. Compared with amplitudes at other periodicities, the yearly 'semiannual' amplitudes in P_e are relatively large compared with the V_{sw} amplitudes in Figs. 5a and 6b.

Because the Lomb–Scargle analysis does not specify the phase of the amplitude peaks, semiannual polynomial fits were made for all daily V_{sw} and P_e data sorted in daynumber. For V_{sw} between 1972 and 2008, we found a semiannual amplitude of 5.7 km/s for equinoctial peaks (22 March and 22 September) and an amplitude of 5.1 km/s for solar axial peaks (6 March and 6 September) with an average V_{sw} of 447 km/s or ~2.6% equinoctial variation. These values are consistent with the 6 km/s equinoctial amplitude found by Cliver et al. (2000) for V_{sw} between 1963 and 1997. The semiannaul equinoctial amplitude for all P_e data was 2.7 GW with an average P_e of 34.5 GW or ~15.7% variation.

Semiannual polynomial fits to V_{sw} and P_e were made for all SC phases. The equinoctial semiannual amplitudes are plotted in the second panel of Fig. 6b, along with solstice semiannual amplitudes that were found for D22, D23 and N23/24. The average V_{sw} equinoctial amplitude from the seven SC phases with equinox peaks over the entire 37 years was ~6.8 km/s (~3.0% variation), similar to the 5.7 km/s found using all V_{sw} data. P_e had equinoctial polynomial peaks for all SC phases except D23, where the solstice V_{sw} variations cancelled out the normal equinoctial peaks in P_e due to preferred magnetospheric reconnection (Cliver et al., 2000). The average equinoctial amplitude in P_e from the other SC phases was ~2.6 GW, close to the 2.7 GW found using all P_e data.

Fig. 7a and b show the daily V_{sw} and P_e during the NA23 period from 95109 to 99270. The Lomb and FFT estimated semiannual and 27-day amplitudes were very similar (as expected) so they were averaged together and plotted on top of annual averages. The lowest annual V_{sw} values were in 1997, while the lowest P_e values were in 1996 and 1997. The 27-day variation was set to agree with the V_{sw} 27-day variation at the start of the minimum period, and so is not correct in the ascending phase, especially when strong CMEs were present, or when a strong 13.5-day periodicity shifted the fit to the 27-day periodicity half a cycle.

The semiannual variation was timed to maximize in the equinoxes since we calculated polynomial equinoctial peaks for both V_{sw} (~19 km/s) and P_e (~5.0 GW) in NA23, which are similar to the Lomb-Scargle semiannual amplitudes in Fig. 6b of ~20 km/s and ~5.3 GW used in Figs. 7a and b. Watari and Watanabe (2000) remarked on the low geomagnetic activity during solstices between 1995 and 1997, with very low values in the solstice of 1996.5, which is also evident in P_e and V_{sw} in Figs. 7b and a.

5. Conclusions

We have shown that the solar wind structure plays a determining role in the magnitude of the electron auroral input as characterized by the hourly average auroral electron power (P_e) over three solar cycles (SCs). The variability in the total magnitude of P_e follows the variations in P_e during periods of high-speed streams (HSS). This is consistent with the similar findings by Richardson et al. (2002) that the variations in the averages of the 3-h *aa* index, the IMF magnitude, and the solar wind velocity closely follow the variations associated only with HSS. Many of the V_{sw} solar periodicities in HSS are transferred to P_e more effectively than in slow-speed solar wind periods, or in times of transients when the periodicities are noisy. This finding about the dominance of HSS in time variations is not too surprising since HSS occur 43% of the time, and the highest velocities, by definition, are during HSS. P_e and *aa* both increase with increasing V_{sw}, although correlations with negative B_z are generally more important.

The characteristics of the hourly average solar wind velocity (V_{sw}) and P_e are similar over the SCs. HSS from coronal holes (CH) contribute ~47% to the total P_e and V_{sw}, and delineate most of the structures seen in both with large 27-day cross-correlations of 0.8 for both. The largest HSS contributions to P_e are ~57% in the descending phases of the SC, with the smallest contributions of ~32% in solar maxima. The slow-speed wind structures contribute ~33% to P_e in solar minima, and ~24% in solar maximum and descending phases.

The contribution of transient (CME) solar wind structures is much more variable. Transients make their maximum contribution during solar maxima (X), contributing ~43% to P_e in X21 and X22, and ~38% in X23 maximum. During solar minimums, transients only contribute ~6% to P_e.

The cross-correlations of $V_{sw}|B|$ in slow-speed wind structures together with HSS with hourly average P_e lagging by 1 h are 0.53 and 0.62 for B_z positive and negative conditions, respectively, and can be represented by linear equations. Because transients represent the largest $|B|$ values, quadratic fits are better, and the cross-correlations of P_e with $V_{sw}|B|$ are lower at 0.47 and 0.56 for B_z positive and negative conditions, respectively. Transients are less effective than other solar wind structures at producing P_e for B_z positive conditions. B_z negative conditions are relatively more important for transients, and the highest hourly cross-correlations of transient P_e are −0.65 with negative $V_{sw}B_z$. The cross-correlations of hourly P_e with 3-h a_p and K_p are higher at 0.68 and 0.72, respectively, for all P_e data from 1978 to 2008.

The solar rotational 27-, 13.5-, 9-, and 7-day periodicities are almost always present in the hourly total V_{sw} and P_e. The magnitudes are usually largest in the descending (D) and minimum (N) phases of each solar cycle. DN23 showed large 7- and 9-day periodicities in V_{sw} and P_e. These same periodicities also appeared in the neutral density at 400 km (Lei et al., 2008a,b; Thayer et al., 2008), and in the power radiated through infrared cooling by $[CO_2]$ and [NO] between 100 and 200 km (Mlynczak et al., 2008).

Relatively weak amplitude 120–145 or 145–165 days periodicities are in the total hourly V_{sw} and P_e. These could be related to the quasi-periodic 150-day periodicities seen in sunspots and other phenomena. Longer periodicities of 270–300 days were relatively common for V_{sw}, and less common for P_e. The 1.3–1.4-year periodicity was found in X22 around 1990 in P_e and V_{sw}.

The 'semiannual' (183 ± 17 day) amplitudes in total hourly V_{sw} were checked with equinoctial polynomial fits. The V_{sw} magnitude at 1 AU is affected by the axial tilt of the Earth's orbit, with the highest heliospheric latitudes seen on 6 March and 6 September. Equinoctial (22 March and 22 September) and axial amplitudes were similar for V_{sw}. The largest equinoctial amplitudes in V_{sw} were for N21/22 (~31 km/s), N22/23 (~21 km/s) and A23 (~16 km/s), with correspondingly high equinoctial amplitudes in P_e of 4.4, 5.1 and 4.9 GW, respectively. Four other SC phases showed V_{sw} equinoctial amplitudes. D22 showed a strong V_{sw} solstice amplitude (~25 km/s), with weaker V_{sw} solstice amplitudes in D23 and N23/24. Equinoctial fits were found in P_e for all SC phases except for D23. The average equinoctial semiannual amplitudes were ~6 km/s (~2.6% variation) in V_{sw} and ~2.7 GW (~15.7% variation) in P_e, where the preferred magnetospheric reconnection at equinoxes (Cliver et al., 2000) greatly enhanced the equinoctial amplitudes in P_e.

The previous six Hale cycles from 10–11 to 20–21 showed higher *aa* indices in DN even cycles and AX odd cycles, except for Hale cycle 16–17 from ~1925 to ~1945 (Cliver et al., 1996). This *aa* pattern was broken again in the last 22–23 Hale cycle (Kozyra et al., 2006) and was relatively weak in Hale cycle 20–21 (Fig. 4 of Cliver et al., 1996). We found the total V_{sw} and P_e values to be usually largest in all D phases because of the dominance of HSS at this time. There was an increase of HSS in N23/24 compared with N22/23 in the abnormal Hale cycle, where the total and HSS V_{sw} magnitudes were increased ~9% from N22/23. However, the P_e magnitudes were about the same because the enhanced V_{sw} was offset by a decrease in IMF magnitude of ~14% in N23/24 compared to N22/23.

Cliver et al. (1996) found the semiannual, 13.5-, 27-day, and the subsidiary 25- and 29-day amplitudes in *aa* to be larger in even SC DN phases compared with AX or odd SC DN phases. We found V_{sw} 13.5-day amplitudes were higher in DN20 compared with DN21, but the other solar rotation amplitudes for V_{sw} and P_e were generally large in all DN phases. In summary, the magnitudes and periodicities of V_{sw} and P_e were generally largest in all D phases where HSS dominate. The expected variations in the Hale cycle are minimal, in part because the 22–23 Hale cycle was unusual.

The very different features of V_{sw} and P_e in every solar cycle are thus explained. The HSS solar velocity sources tend to drive the observed average variations of both the total V_{sw} and the total P_e and their solar periodicities, although they only account for approximately half of the total frequency and fraction of solar structure occurrences.

Acknowledgments

This material is based upon work supported by the National Science Foundation under Space Weather Grant no. 0208145 with additional support from the National Aeronautics and Space Administration (NASA) Living with a Star Grant no. NNH05AB54I. The original DMSP and NOAA satellite hemispheric power estimates were taken from the CEDAR Database, which is supported by the National Science Foundation. The hourly solar wind plasma and IMF data were taken from the OMNI-2 collection from the Space Physics Data Facility at the Goddard Space Flight Center managed by Dr. Natalia Papitashvili. IGR is supported by a NASA heliophysics guest investigator grant.

References

Ahluwalia, H.S., 2000. A_p time variations and interplanetary magnetic field intensity. J. Geophys. Res. 105, 27481–27487.

Belcher, J.W., Davis, L., 1971. Large amplitude Alfven waves in the interplanetary medium, 2. Journal of Geophysical Research 76 (16), 3543–3563.

Berdichevsky, D.B., Richardson, I.G., Lepping, R.P., 2005. On the origin and configuration of the 20 March 2003 interplanetary shock and magnetic cloud at 1 AU. Journal of Geophysical Research 110, A09105, doi:10.1029/2004JA010662.

Bohlin, J.D., 1977. Extreme-ultraviolet observations of coronal holes. Solar Physics 51, 377–398.

Borrini, G., Gosling, J.T., Bame, S.J., Feldman, W.C., 1982. Helium abundance enhancements in the solar wind. Journal of Geophysical Research 87, 7370–7378.

Brautigam, D.H., Gussenhoven, M.S., Hardy, D.A., 1991. A statistical study on the effects of IMF B_z and solar wind speed on aurora ion and electron precipitation. Journal of Geophysical Research 96, 5525–5538.

Cane, H.V., 1988. The large-scale structure of flare-associated interplanetary shocks. Journal of Geophysical Research 93, 1–6.
Cane, H.V., Richardson, I.G., 2003. Interplanetary coronal mass ejections in the near-Earth solar wind during 1996–2002. Journal of Geophysical Research 108(4), doi:10.1029/2002JA009817.
Cane, H.V., Richardson, I.G., von Rosenvinge, T.T., 1996. Cosmic ray decreases: 1964–1994. Journal of Geophysical Research 101, 21S61–21S72.
Charan Dwivedi, V., Tiwari, D.P., Agrawal, S.P., 2009. Study of the long-term variability of interplanetary plasma and fields as a link for solar–terrestrial relationships. J. Geophys. Res. 114, A0S108, doi:10.1029/2009JA014171.
Cliver, E.W., Boriakoff, V., 8ounar, K.H., 1996. The 22-year cycle of geomagnetic and solar wind activity. Journal of Geophysical Research 101 (A12), 27091–27109.
Cliver, E.W., Kamide, Y., Ling, A.G., 2000. Mountains versus valleys: semiannual variation of geomagnetic activity. Journal of Geophysical Research 10S, 2413–2424.
Crooker, N.U., Feynman, J., Gosling, J.T., 1977. On the high correlation between long-term averages of solar wind speed and geomagnetic activity. J. Geophys. Res. 82, 1933–1937.
Delouis, H., Mayaud, P.N., 1975. Spectral analysis of the geomagnetic activity index *aa* over a 103-year interval. Journal of Geophysical Research 80, 4681–4688.
Emery, 8.A., Evans, D.S., Greer, M.S., Kadinsky-Cade, K., Holeman, E., Rich, F.J., Xu, W., 200S. NOAA and DMSP intersatellite adjusted hemispheric power data sets, described at 〈http://cedarweb.hao.ucar.edu/wiki/index.php/Instruments:ehp〉 in the Coupling, Energetics and Dynamics of Atmospheric Regions (CEDAR) Database at the National Center for Atmospheric Research (NCAR), 8oulder, CO, USA (revised in 200B).
Emery, 8.A., Evans, D.S., Greer, M.S., Holeman, E., Kadinsky-Cade, K., Rich, F.J., Xu, W., 2006. The low energy auroral electron and ion hemispheric power after NOAA and DMSP intersatellite adjustments. NCAR Scientific and Technical Report, TN-470+STR (〈http://cedarweb.hao.ucar.edu/wiki/index.php/Media:Str470.pdf〉 in the CEDAR Database or available through the NCAR library at 〈http://library.ucar.edu〉).
Emery, B.A., Coumans, V., Evans, D.S., Germany, G.A., Greer, M.S., Holeman, E., Kadinsky-Cade, K., Rich, F.J., Xu, W., 2008. Seasonal, K_p, solar wind, and solar flux variations in long-term single pass satellite estimates of electron and ion auroral hemispheric power. Journal of Geophysical Research 113, A06311, doi:10.1029/2007JA012866.
Fuller-Rowell, T.J., Evans, D.S., 1987. Height-integrated Pedersen and Hall conductivity patterns inferred from the TIROS/NOAA satellite data. Journal of Geophysical Research 92, 7606–761B.
Gibson, S.E., Kozyra, J.U., de Toma, G., Emery, 8.A., Onsager, T., Thompson, 8.J., 2009. If the Sun is so quiet, why is the Earth ringing? A comparison of two solar minimum intervals. J. Geophys. Res. 114, in press.
Gonzalez, W.D., Gonzalez, A.L.C., Tsurutani, 8.T., 1990. Dual-peak cycle distribution of intense geomagnetic storms. Planetary and Space Sciences 3B, 1B1–1B7.
Gonzalez, W.D., Joselyn, J.A., Kamide, Y., Kroehl, H.W., Rostoker, G., Tsurutani, 8.T., Vsyliunas, V.M., 1994. What is a geomagnetic storm? Journal of Geophysical Research 99, S771–S792.
Gorney, D.J., 1990. Solar cycle effects on the near-Earth space environment. Reviews of Geophysics 28, 31S–336.
Gosling, J.T., Asbridge, J.R., Bame, S.J., Feldman, W.C., 1976. Solar wind speed variations: 1962–1974. Journal of Geophysical Research B1, S061–S070.
Gosling, J.T., Asbridge, J.R., Bame, S.J., Feldman, W.C., 1977. Preferred solar wind emitting longitudes on the sun. Journal of Geophysical Research 82, 2371–2376.
Hale, G.E., Nicholson, S.B., 192S. The law of sun-spot polarity. Astrophysical Journal 62, 270–300.
Hamrin, M., Norqvist, P., Rönnmark, K., Fellgård, D., 200S. The importance of solar illumination for discrete and diffuse aurora. Annales Geophysicae 23, 3481–3486.
Hardy, D.A., Gussenhoven, M.S., Holeman, E., 198S. A statistical model of auroral precipitation. Journal of Geophysical Research 90, 4229–4248.
Hardy, D.A., Gussenhoven, M.S., Brautigam, D., 1989. A statistical model of auroral ion precipitation. Journal of Geophysical Research 94, 370–392.
Harrington, J., Dowling, T.E., Baron, R.L., 1996. Jupiter's tropospheric thermal emission, II. Power spectrum analysis and wave search. Icarus 124, 32–44.
Hasegawa, H., Sonnerup, 8.U.Ö., Owen, C.J., Klecker, 8., Paschmann, G., Balogh, A., Rème, H., 2006. The structure of flux transfer events recovered from Cluster data. Ann. Geophys. 24, 603–618.
Hubert, 8., Gérard, J.-C., Evans, D.S., Meurant, M., Mende, S.8., Frey, H.U., Immel, T.J., 2002. Total electron and proton energy input during auroral substorms: remote sensing with IMAGE-FUV. Journal of Geophysical Research 107, A8, doi:10.1029/2001JA009229.
Iijima, T., Potemra, T.A., 1976. The amplitude distribution of field-aligned currents at northern high latitudes observed by Triad. Journal of Geophysical Research 81, 216S–2174.
Javaraiah, J., Bertello, L., Ulrich, R.K., 200S. An interpretation of the differences in the solar rotation during even and odd sunspot cycles. Astrophysical Journal 626, S79–S84.
Jian, L., Russell, C.T., Luhmann, J.G., Skoug, R.M., 2006a. Properties of stream interactions at one AU during 199S–2004. Solar Physics 239, 337–392.
Jian, L., Russell, C.T., Luhmann, J.G., Skoug, R.M., 2006b. Properties of interplanetary coronal mass ejections at one AU during 199S–2004. Solar Physics 239, 393–436.
Kozyra, J.U., Crowley, G., Emery, B.A., Fang, X.H., Maris, G., Mlynczak, M.G., Niciejewski, R.J., Palo, S.E., Paxton, L.J., Randall, C.E., Rong, P.-P., Russell III, J.M., Skinner, W., Solomon, S.C., Talaat, E.R., Wu, Q., Yee, J.-H., 2006. Response of the upper/middle atmosphere to coronal holes and powerful high-speed solar wind streams in 2003. In: Tsurutani, 8.T., McPherron, R.L., Gonzalez, W.D., Lu, G., Sobral, J.H.A., Gopalswamy, N. (Eds.), Recurrent Magnetic Storms: Corotating Solar Wind Streams. Geophysical Monograph Series 167. American Geophysical Union, pp. 319–340.
Laguna, P., Moody, G.8., Marck, R.G., 1998. Power spectral density of unevenly sampled data by least-square analysis: performance and application to heart rate signals. IEEE Transactions on 8iomedical Engineering S (6), 698–71S.
Lean, J.L., 1990. Evolution of the 155 day periodicity in sunspot areas during solar cycles 12 to 21. Astrophysics Journal 363, 718–727.
Lei, J., Thayer, J.P., Forbes, J.M., Sutton, E.K., Nerem, R.S., 2008a. Rotating solar coronal holes and periodic modulation of the upper atmosphere. Geophysical Research Letters 3S, L10109, doi:10.1029/200BGL033B75.
Lei, J., Thayer, J.P., Forbes, J.M., Sutton, E.K., Nerem, R.S., Temmer, M., Veronig, A.M., 2008b. Global thermospheric density variations caused by high-speed solar wind streams during the declining phase of solar cycle 23. J. Geophys. Res. 113, A11303, doi:10.1029/2008JA013433.
Li, Y., Luhmann, J., 2004. Solar cycle control of the magnetic cloud polarity and the geoeffectiveness. Journal of Atmospheric and Solar-Terrestrial Physics 66, 323–331.
Lindblad, 8.A., 19B1. Preferred Bartels days of high-speed plasma streams in the solar wind. Solar Phys. 74, 187–196.
Lindblad, 8.A., Lundstedt, H., Larsson, B., 19B9. A third catalogue of high-speed plasma streams in the solar wind—data for 197B–1982. Solar Physics 120, 14S–1S2.
Lindsay, G.M., Luhmann, J.G., Russell, C.T., Gosling, J.T., 1999. Relationship between coronal mass ejection speeds from coronagraph images and interplanetary characteristics of the associated interplanetary coronal mass ejections. Journal of Geophysical Research 104, 12S1S–12S23.
Liou, K., Newell, P.T., Meng, C.-I., 8rittnacher, M., Parks, G., 1998. Characteristics of the solar wind controlled auroral emissions. Journal of Geophysical Research 103, 17S43–17SS7.
Lomb, N.R., 1976. Least-squares frequency analysis of unequally spaced data. Astrophysical and Space Science 39, 447–462.
Luan, X., Wang, W., 8urns, A.G., Solomon, S.C., Zhang, Y., Paxton, L.J., 2009. The unusual declining phase of solar cycle 23: weak semi-annual variations of auroral hemispheric power and geomagnetic activity. Geophys. Res. Lett. 36, under revision.
Lui, A.T.Y., Sibeck, D.G., Phan, T., McFadden, J.P., Angelopoulos, V., Glassmeier, K.-H., 2008. Reconstruction of a flux transfer event based on observations from five THEMIS satellites. J. Geophys. Res. 113, A00C01, doi:10.1029/2008JA013189.
Lummerzheim, D., 8rittnacher, M., Evans, D., Germany, G.A., Parks, G.K., Rees, M.H., Spann, J.F., 1997. High time resolution study of the hemispheric energy flux carried by energetic electrons into the ionosphere during the May 19/20 auroral activity. Geophysical Research Letters 24, 987–990.
Makarov, V.I., Sivaraman, K.R., 1989. Evolution of latitude zonal structure of the large-scale magnetic field in solar cycles. Solar Physics 119, 3S–SS.
Maris, O., Maris, G., 2005. Specific features of the high-speed plasma stream cycles. Advances in Space Research 3S, 2129–2140.

Mavromichalaki, H., Vassilaki, A., 1998. Fast plasma streams recorded near the Earth during 1985–1996. Solar Physics 183, 181–200.
Mavromichalaki, H., Vassilaki, A., Marmatsouri, E., 1988. A catalogue of high-speed solar-wind streams: further evidence of their relationship to A_p-index. Solar Physics 115, 345–365.
Mavromichalaki, H., Vassilaki, A., Tsagouri, I., 1999. Sector-structured interplanetary magnetic field associated with the fast plasma streams in 1985–1996. Solar Physics 189, 199–216.
Mlynczak, M.G., Martin-Torres, F.J., Mertens, C.J., Marshall, B.T., Thompson, R.E., Kozyra, J.U., Remsberg, E.E., Gordley, L.L., Russell III, J.M., Woods, T., 2008. Solar–terrestrial coupling evidenced by periodic behavior in geomagnetic indexes and the infrared energy budget of the thermosphere. Geophysical Research Letters 35, L05808, doi:10.1029/2007GL032620.
Mursula, K., Zieger, B., 1996. The 13.5-day periodicity in the sun, solar wind, and geomagnetic activity: the last three solar cycles. Journal of Geophysical Research 101, 27077–27090.
Nayar, S.R.P., Nair, V.S., Radhika, V.N., Revathy, K., 2001. Short-period features of the interplanetary plasma and their evolution. Solar Physics 201, 405–417.
Neugebauer, M., Smith, E.J., Ruzmaikin, A., Feynman, J., Vaughan, A.H., 2000. The solar magnetic field and the solar wind: existence of preferred longitudes. Journal of Geophysical Research 105, 2315–2324.
Prestes, A., Rigozo, N.R., Echer, E., Vieira, L.E.A., 2006. Spectral analysis of sunspot number and geomagnetic indices (1868–2001). Journal of Atmospheric and Solar-Terrestrial Physics 68, 182–190.
Raeder, J., 2006. Flux transfer events: 1. Generation mechanism for strong southward IMF. Ann. Geophys. 24, 381–392.
Rangarajan, G.K., Mavromichalaki, H., 1989. Preferred Bartels days of high speed solar wind streams: an update. Solar Physics 122, 187–189.
Reiff, P.H., Luhmann, J.G., 1986. Solar wind control of the polar-cap voltage. In: Kamide, Y., Slavin, J.A. (Eds.), Proceedings of Solar Wind-Magnetosphere Coupling. Terra Scientific Publishing Company, pp. 453–476.
Richardson, I.G., Cane, H.V., 1993. Signatures of shock drivers in the solar wind and their dependence on the solar source location. Journal of Geophysical Research 98, 15295–15304.
Richardson, I.G., Cane, H.V., 1995. Regions of abnormally low proton temperature in the solar wind (1965–1991) and their association with ejecta. Journal of Geophysical Research 100, 23397–23412.
Richardson, I.G., Cane, H.V., 2005. The ~150 day quasi-periodicity in interplanetary and solar phenomena during cycle 23. Geophysical Research Letters 32, L02104, doi:10.1029/2004GL021691.
Richardson, J.D., Paularena, K.I., Belcher, J.W., Lazarus, A.J., 1994. Solar wind oscillations with a 1.3 year period. Geophysical Research Letters 21 (14), 1559–1560.
Richardson, I.G., Wibberenz, G., Cane, H.V., 1996. The relationship between recurring cosmic ray depressions and corotating soar wind streams at <1 AU: IMP 8 and Helios 1 and 2 anti-coincidence guard rate observations. Journal of Geophysical Research 101, 13483–13496.
Richardson, I.G., Farrugia, C.J., Cane, H.V., 1997. A statistical study of the electron temperature in ejecta. Journal of Geophysical Research 102, 4691–4699.
Richardson, I.G., Cliver, E.W., Cane, H.V., 2000. Sources of geomagnetic activity over the solar cycle: relative importance of coronal mass ejections, high-speed streams, and slow solar wind. Journal of Geophysical Research 105, 18203–18213.
Richardson, I.G., Cliver, E.W., Cane, H.V., 2001. Sources of geomagnetic storms for solar minimum and maximum conditions during 1972–2000. Geophysical Research Letters 28 (13), 2569–2572.
Richardson, I.G., Cane, H.V., Cliver, E.W., 2002. Sources of geomagnetic activity during nearly three solar cycles (1972–2000). Journal of Geophysical Research 107(8), doi:10.1029/2001JA000504.
Rosenberg, R.L., Coleman, P.J., 1969. Heliographic latitude dependence of the dominant polarity of the interplanetary magnetic field. Journal of Geophysical Research 74, 5611–5622.
Russell, C.T., McPherron, R.L., 1973. Semiannual variation of geomagnetic activity. Journal of Geophysical Research 78, 92–108.
Scargle, J.D., 1982. Studies in astronomical time series analysis, II. Statistical aspects of spectral analysis of unevenly spaced data. Astrophysical Journal 253, 835–853.
Shue, J.-H., Newell, P.T., Liou, K., Meng, C.-I., 2001. Influence of interplanetary magnetic field on global auroral patterns. Journal of Geophysical Research 106, 5913–5926.
Silverman, S.M., Shapiro, R., 1983. Power spectral analysis of auroral occurrence frequency. Journal of Geophysical Research 88 (A8), 6310–6316.
Svalgaard, L., Wilcox, J.W., 1975. Long term evolution of solar sector structure. Solar Physics 41, 461–475.
Temmer, M., Vrsnak, B., Veronig, A.M., 2007. Periodic appearance of coronal holes and the related variation of solar wind parameters. Solar Physics 241, 371–383.
Thayer, J.P., Lei, J., Forbes, J.M., Sutton, E.K., Nerem, R.S., 2008. Thermospheric density oscillations due to periodic solar wind high speed streams. J. Geophysical Research 113, A06307, doi:10.1029/2008JA013190.
Thong, T., McNames, J., Aboy, M., Oken, B., 2004. Averaged Lomb periodograms for nonuniform sampling. BIOSIGNAL 2004 publications at Biomedical Signal Processing (BSP) Laboratory at Portland State University, BIOSIGNAL2004 ⟨http://bsp.pdx.edu/Publications/2004/BIOSIGNAL_Thong.pdf⟩.
Tsurutani, B.T., Gonzalez, W.D., Gonzalez, A.L.C., Tang, F., Arballo, J.K., Okada, M., 1995. Interplanetary origin of geomagnetic activity in the declining phase of the solar cycle. J. Geophys. Res. 100, 21717–21733.
Verma, V.K., 2001. On the periodicity of high speed solar wind streams. Space Science Reviews 97, 205–210.
Vityazev, V.V., 1997. Time series analysis of unequally spaced data: intercomparison between estimators of the power spectrum. In: Hunt, G., Payne, H.E. (Eds.), Astronomical Data Analysis Software and Systems VI, ASP Conference Series, vol. 125.
Watari, S., Watanabe, T., 2000. High-speed streams from coronal holes and coronal mass ejections around the solar minimum of cycle 22. Advances in Space Research 25, 1863–1866.
Zhang, J., Richardson, I.G., Webb, D.F., Gopalswamy, N., Nuttunen, E., Kasper, J.C., Nitta, N.V., Poomvises, W., Thompson, B.J., Wu, C.-C., Yashiro, S., Zhukov, A.N., 2007. Solar and interplanetary sources of major geomagnetic storms ($D_{ST}<-100$ nT) during 1996–2005. Journal of Geophysical Research 112, A10102, doi:10.1029/2007JA012321.
Zhang, Y., Paxton, L.J., 2008. An empirical K_p-dependent global auroral model based on TIMED/GUVI FUV data. J. Atmos. Terr. Phys. 70, doi:10.1016/jastp.2008.03.008.
Zurbuchen, T.H., Richardson, I.G., 2006. In-situ solar wind and magnetic field signatures of interplanetary coronal mass ejections. Space Science Reviews 123, 31–43.